

## Technical Articles

- Direct Solid-State Electrochemical De-oxidation of Metal Oxides to Metal – An Overview
- Development of Next Generation Instrumentation & Control Systems using Indigenous Real-Time Operating System for FBRs

## Young Officer's Forum

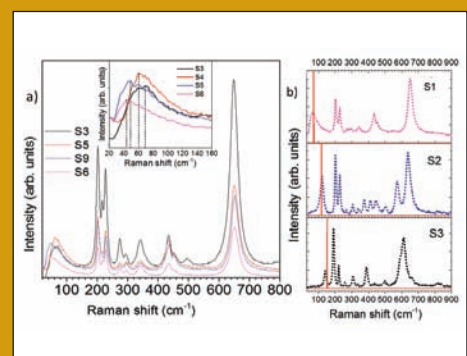
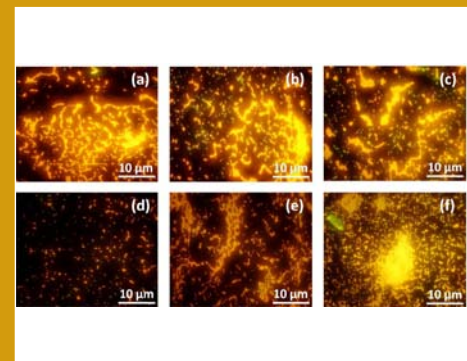
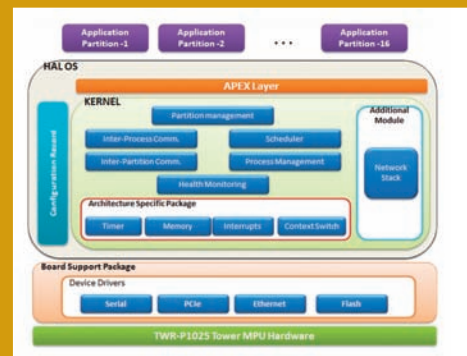
- Enhanced Corrosion Resistance and Photocatalytic Activity of Thermally Oxidized Titanium: Role of Titania Film Thickness, Topography and Phase Composition

## Young Researcher's Forum

- First Observation of Spin Wave in Vanadium dioxide
- Measures related to COVID-19

## HBNI-IGCAR Corner

## Awards & Honours



## *From the Editorial Committee*

### *Dear Reader*

It is our pleasant privilege to forward a copy of the latest issue of IGC Newsletter (Volume 126, October 2020 issue).

In the first technical article, Dr. R. Kumaresan and colleagues from Materials Chemistry & Metal Fuel Cycle Group have discussed about the “Direct Solid-State Electrochemical De-oxidation of Metal Oxides to Metal – An Overview”.

In the second technical article, Ms. T. Jayanthi and colleagues from Electronics & Instrumentation Group have discussed about the “Development of Next Generation Instrumentation & Control Systems using Indigenous Real-Time Operating System for FBRs”.

Shri D. Nanda Gopala Krishna, Metallurgy & Materials Group has described about the “Enhanced Corrosion Resistance and Photocatalytic Activity of Thermally Oxidized Titanium: Role of Titania Film Thickness, Topography and Phase Composition” in the Young Officer’s Forum.

This issue’s Young Researcher’s Forum features an article by Dr. Raktima Basu, Materials Science Group, IGCAR discussing about “First Observation of Spin Wave in Vanadium dioxide”.

We are happy to share with you the awards, honours and distinctions earned by our colleagues.

We look forward to your comments, continued guidance and support.

With best wishes and personal regards

Editorial Committee, IGC Newsletter

## Direct Solid-State Electrochemical De-oxidation of Metal Oxides to Metal – An Overview

Metals and alloys have played a very important role in the advancement of human civilization. Most of the metals existed on earth's crust as metal compounds and are converted to metals by strong reducing agents like calcium, magnesium and lithium or carbon. Discovery of electrochemical processes for metal production enabled extraction of many metals that are difficult to be obtained by the conventional chemical reduction method due to the high stability of the metal compounds. For example, many reactive metals like sodium, potassium, lithium, magnesium and calcium have been produced by electrolysis of the respective fused chlorides. Molten salt electrolysis has evolved as an efficient and economical method for producing metals from highly stable metal compounds.

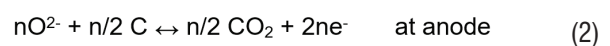
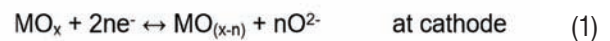
Solid-state electrochemical de-oxidation of metal oxides to metals in high temperature molten salt medium, by electrons [Fray-Farthing-Chen (FFC) Cambridge process] or by in-situ generated electro-positive metals like lithium and calcium (electro-metallothermic reduction process) has been a new development in electrometallurgy for production of metals and alloys. In FFC Cambridge process, electrons serve as the reductant whereas in electro-metallothermic method, a strong reductant metal like lithium or calcium, generated in-situ from the molten electrolyte medium by electrolysis, serves as the reductant. In both the cases, the solid metal oxide, which is in contact with current conducting metal part, forms the cathode in the electrolytic cell and the oxygen present in it is removed as  $O^{2-}$  ions to obtain the metal. In course of time, the solid metal oxide electrode transforms to the corresponding metal. The salient features of the solid-state electrochemical processes are briefly explained below.

### FFC Cambridge process

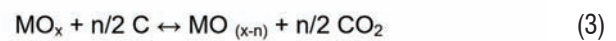
FFC Cambridge process is a molten salt electrochemical deoxidation method that was invented at University of Cambridge two decades ago. It is a generic technology that involves the direct conversion of solid metal oxides into the corresponding metals or alloys through cathodic polarisation of the oxide in molten calcium chloride. The process has witnessed significant progresses in many aspects, including commercialization and laboratory demonstrations with technological advancements over the past two decades. In this process, a single oxide or a mixture of oxides is prepared as a solid pre-form and configured as the cathode in the electrochemical cell with calcium chloride melt at 900-950°C. Graphite serves as the anode. A constant voltage of 3.0 or 3.1 V is applied across the

electrodes and the  $O^{2-}$  ions from metal oxides are discharged at the graphite anode as  $CO_2$  or  $CO$ . As the process is continued, the oxide electrode is converted to the corresponding metal. The overall cathode reaction is simply the ionization of the oxygen and the ionized oxygen transports to anode and discharges as  $CO_2/CO$ . The cell reactions are represented in equations 1 to 4.

Cell reactions:



Net reaction:



For anodic evolution of  $CO$ , the equation can be written as



A unique feature of FFC Cambridge process is that electro-deoxidation of metal oxide occurs at an applied potential, which is lower than the decomposition potential of the electrolyte. For example, in molten  $CaCl_2$  the de-oxidation process occurs at a potential less than 3.2 V (decomposition potential of  $CaCl_2$  at 900°C is 3.21 V). The reduction is considered to occur by the "oxygen ionization mechanism". The process also enables production of alloys, when the oxide electrode is prepared from a mixture of metal oxides. The schematic of the process is given in Figure 1.

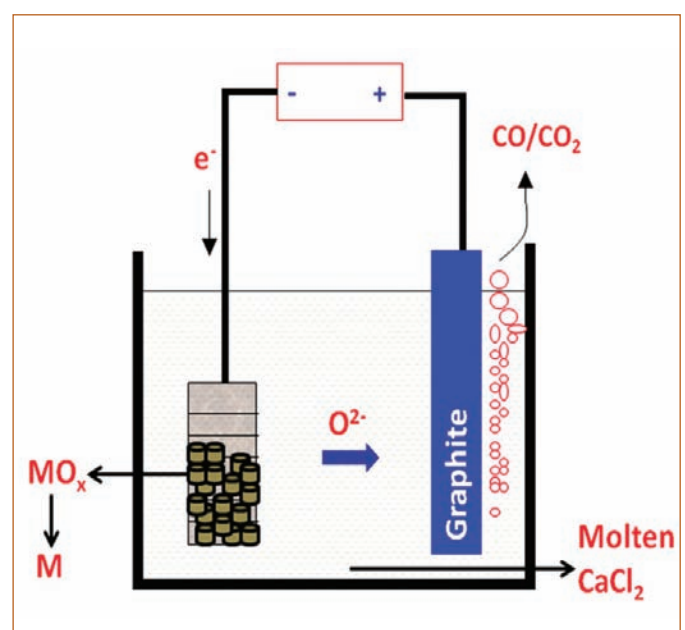


Figure 1: Schematic diagram of FFC Cambridge Process

### Electro-metallothermic reduction process

In this process, a reductant metal is electro-generated (in-situ) on the solid metal oxide electrode which is configured as the cathode in the cell and the reductant metal chemically reduces the oxide to metal. The reductant metal is usually highly electropositive in nature. For example, lithium and calcium are often used for this purpose. In the electro-lithiothermic reduction process, LiCl melt containing 0.5-3 wt.% Li<sub>2</sub>O is used as the electrolyte and in the electro-calciothermic process, molten calcium chloride containing 0.5-1 wt.% CaO is used as the electrolyte. Electrolysis of the dissolved oxide (Li<sub>2</sub>O and CaO), generates metals (Li, Ca) necessary for their reduction of the solid oxide. Platinum is used as the anode in electro-lithiothermic reduction process while graphite is used as the anode in the electro-calciothermic process. Solubility of lithium metal in LiCl melt is very low (0.4 mol.% at 650 °C) and therefore the metal deposited on the oxide electrode remains there for sufficient period of time for the reduction reaction to take place. However, in the case of calciothermic reduction, solubility of calcium metal in calcium chloride melt is high (4 mol.% at 900 °C) and this makes the electro-deposited calcium dissolve quite fast into the melt. The chemical and electrochemical processes governing the electro-metallothermic reduction process are given in Table 1.

### Unique features of solid state electrochemical-reduction process

Direct solid-state electrochemical reduction processes are unique compared to conventional chemical and electrochemical metal production processes. In conventional electrolytic process, the metal compound is dissolved in an electrolyte medium and electrolysed to obtain metals. In these processes, the metal oxide is not dissolved in the electrolyte melt, but exists as solid (pre-form or powder) at the cathode in contact with the molten electrolyte. The de-oxidation of the metal oxide takes place in one step, whereas in the conventional chemical reduction, the metal oxide is first converted to a metal halide and the halide is subsequently

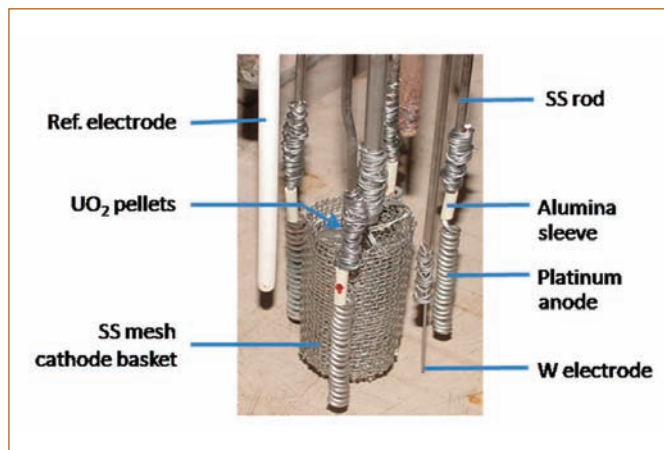


Figure 2: The electrode arrangement inside the electrolysis cell. Four platinum anodes are placed radially around the cathode basket containing UO<sub>2</sub> pellets

reduced to the metal with the help of a reductant metal. The two step process becomes necessary to avoid contamination of the freshly reduced metal with oxygen. Obviously, the metal production in a single step in electro-deoxidation processes offers significant advantages over the two-step conventional reduction processes. As the electrolysed metal product remains as solid at the cathode, its recovery from the cell becomes relatively easy compared to that from conventional chemical and electrochemical reactors.

A glimpse of the work carried out in our laboratory in the area of direct solid-state metal oxide reduction is presented in this article. Some representative results obtained in different metal oxide reductions are briefly discussed in the following sections.

### Electro-lithiothermic reduction of UO<sub>2</sub>

Uranium dioxide is the major constituent of spent oxide nuclear fuel and hence in the context of pyroprocessing, electrochemical reduction process has been investigated in detail. The basic studies to understand the fundamentals of electrochemical reduction behavior of UO<sub>2</sub> with pellets weighing about a gram was initially carried out and gradually the process was

Table 1: Electrochemical and chemical processes governing electro-metallothermic reduction

Cell: Pt (s)/LiCl, Li <sub>2</sub> O(l)/MO <sub>x</sub> (s)	Cell: C(s)/CaCl <sub>2</sub> , CaO(l)/MO <sub>x</sub> (s)
At cathode: 2nLi <sup>+</sup> + 2ne <sup>-</sup> → 2nLi (electrochemical) MO <sub>x</sub> + 2nLi ↔ MO <sub>(x-n)</sub> + 2nLi <sup>+</sup> + nO <sup>2-</sup> (chemical)	At cathode: nCa <sup>2+</sup> + 2ne <sup>-</sup> → nCa (electrochemical) MO <sub>x</sub> + nCa → MO <sub>(x-n)</sub> + nCa <sup>2+</sup> + nO <sup>2-</sup>
At platinum anode: nO <sup>2-</sup> → n/2 O <sub>2</sub> (g) + 2ne <sup>-</sup>	At graphite anode: nO <sup>2-</sup> + n/2 C ↔ n/2 CO <sub>2</sub> (g) + 2ne <sup>-</sup>
Net reaction: MO <sub>x</sub> → MO <sub>(x-n)</sub> + n/2 O <sub>2</sub>	Net reaction: MO <sub>x</sub> + n/2 C → MO <sub>(x-n)</sub> + n/2 CO <sub>2</sub>

upgraded/developed for the reduction of 200g batches of  $UO_2$ , with a reduction efficiency of  $\sim 98\%$ . The reduced pellets were distilled under vacuum at  $900^\circ C$  to remove the adhering salt and subsequently electrorefined in LiCl-KCl eutectic melt at  $500^\circ C$  to obtain the pure U metal.

Details of a typical electro-reduction experiment carried out with 100g  $UO_2$  pellets in LiCl-1wt.%  $Li_2O$  melt with platinum anode at  $650^\circ C$ , are discussed below.

### Electrochemical reduction experiments with 100 g $UO_2$ pellets

Cyclic Voltammetry (CV) measurements conducted in the melt provided the potentials for lithium deposition on W electrode, oxygen evolution on platinum electrode and platinum dissolution as  $-2.3$  V,  $+0.5$  V to  $+1.4$  V, and  $+1.4$  V respectively against Ni/NiO reference electrode. From this data, it was obvious that the platinum anode potential should be above  $+0.5$  V and below  $+1.4$  V for the electro-reduction to occur without anodic dissolution of platinum in the melt and cathodic potential has to be more than  $-2.3$  V to deposit lithium. The  $UO_2$  pellets of dimension 6 mm dia. x 6 mm height were taken in a SS mesh basket and four platinum coil electrodes (2 mm diameter) were used as the anodes. The arrangement of electrodes inside the cell is shown in Figure 2.

A cathodic potential of  $-2.3$  V was achieved by passing a constant current of 10 A, which made Li metal deposit on the  $UO_2$  cathode. The electro-lithiothermic reduction of  $UO_2$  to U took place by two steps as per the following two reactions (Equations 5 and 6), one through electrochemical and the other through chemical route.

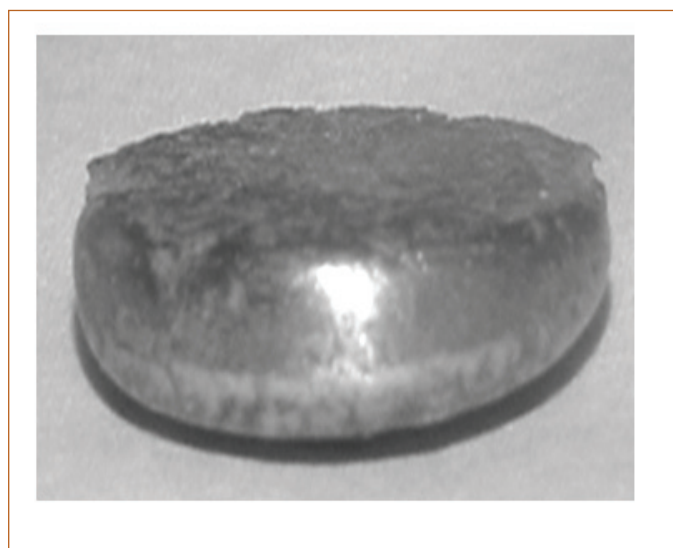


Figure 3: A portion of consolidated U metal by induction melting technique

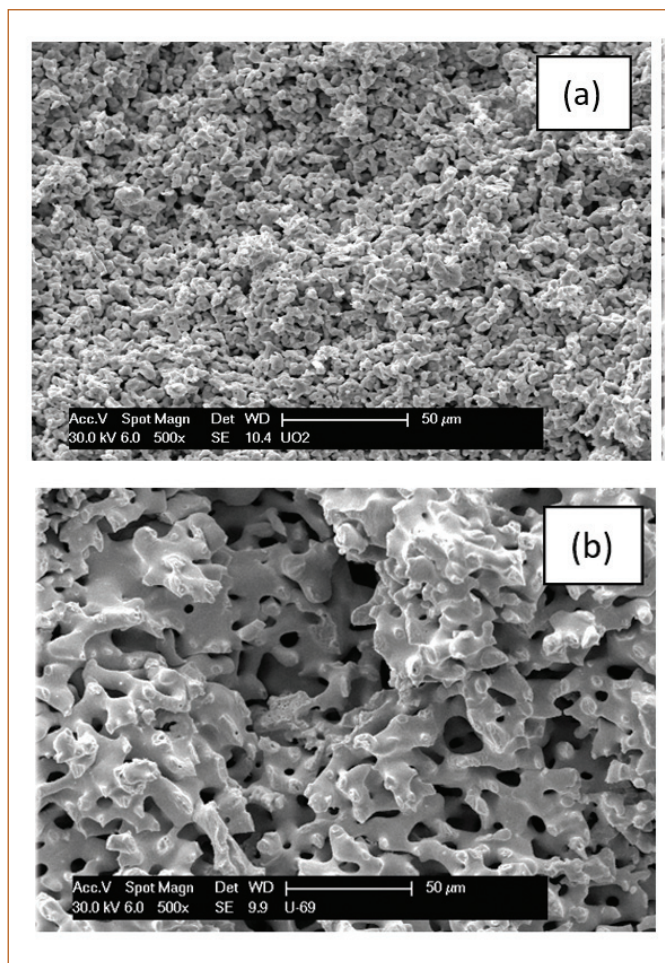


Figure 4: SEM images of fractured surface of (a) original  $UO_2$  pellet and (b) the electro-reduced U metal



The deposition of lithium on the  $UO_2$  pellets and allowing time for its reaction with  $UO_2$  by interruption of the cell current were continued until the pellets were converted to U metal. The cell was allowed to cool to room temperature and the cathode basket containing electro-reduced U metal was removed from the cell. The cathode basket was cut to remove the electrolysed U metal with significant amount of the LiCl salt adhering to it. The product after electrolysis was vacuum distilled at  $900^\circ C$  in an in-house fabricated vacuum distillation vessel to distill the adhered LiCl salt (about 20 - 30 wt%) and to collect the U metal produced. U metal content in the electrolysis product was analyzed quantitatively by measuring the volume of hydrogen gas produced in a gas burette by reacting it with 48% HBr. The hydrogen was also estimated using an in-house developed polymer hydrogen sensor. It was found to contain  $\sim 98\%$  U metal and the rest unreduced  $UO_2$ . The impure product was then electro-refined in a bath of LiCl-KCl-5

wt%  $\text{UCl}_3$  to prepare pure U metal. The impure metal was taken as the anode in the electro-refiner against a steel rod cathode. On application of a small potential difference between the electrodes, U metal got deposited on the steel cathode in the form of dendrites. The U dendrites were then vacuum-distilled at  $900^\circ\text{C}$  to remove occluded salts and the salt-free metal was induction-melted to get a pure U metal ingot. The consolidated U metal (about 65 g) is shown in Figure 3. The SEM images of the fractured surface of original  $\text{UO}_2$  pellet and that of the electrolyzed product are given in Figure 4a and 4b respectively. A molten salt experimental facility is being built up at present to carry out electrochemical reduction of  $\text{UO}_2$  and other oxides in kilogram scale.

### Electro-lithiothermic reduction of $\text{ZrO}_2$

Zirconium is an essential element for the preparation of many alloys. In nuclear context, the reduction of  $\text{ZrO}_2$  to Zr gained importance in the development of metallic fuels and pyroprocessing of spent oxide nuclear fuels. The reduction of  $\text{ZrO}_2$  to Zr in  $\text{LiCl-Li}_2\text{O}$  melt is reported as very difficult due to the formation of intermediate compound,  $\text{Li}_2\text{ZrO}_3$ , which is considered to resist the reduction. We have taken up the study on electro-reduction of  $\text{ZrO}_2$  in this backdrop. Powder compacted and sintered  $\text{ZrO}_2$  pellet, (i) wound around with SS wire and (ii) placed in SS mesh basket were the two kinds of cathode assemblies used in the study. Pure  $\text{LiCl}$  and  $\text{LiCl}$  containing varying quantities, up to 1wt.%, of  $\text{Li}_2\text{O}$  were used for different experiments. Graphite was used as anode for the melt compositions,  $\text{LiCl}$  (0-0.5) wt.%  $\text{Li}_2\text{O}$  and platinum for the compositions,  $\text{LiCl}$ -(0.5,1) wt.%  $\text{Li}_2\text{O}$ . About two times of charge compared to that theoretically required for reduction of  $\text{ZrO}_2$  was passed through the cell. The pellet was electro-reduced to Zr metal in all melt compositions, but minor amount of  $\text{Li}_2\text{ZrO}_3$  was also present in the samples reduced in the  $\text{Li}_2\text{O}$  containing melts. This indicated that the formation of ternary compound could be possible in  $\text{Li}_2\text{O}$  containing melts. The results of some

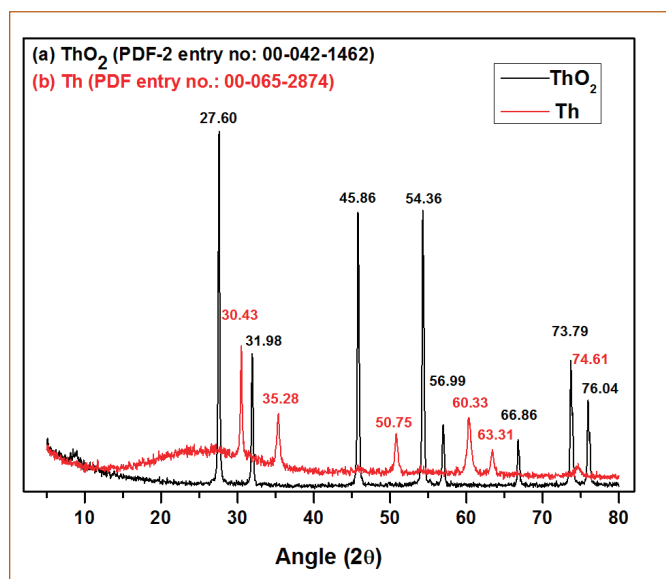


Figure 6: The XRD patterns of sintered  $\text{ThO}_2$  pellet before and after electrochemical reduction

of the representative experiments carried out are given in Table 2. It showed that the oxide was reduced to Zr and minor quantity of  $\text{Li}_2\text{ZrO}_3$  was also present in the reduced sample.

Table 2: Details of experiments and results of analysis of the reduction products of  $\text{ZrO}_2$  electrolysis in  $\text{LiCl-Li}_2\text{O}$  melt using platinum and graphite anodes.

Melt	Current (A)	Charge passed (Ah)	Anode	Phases identified in XRD analysis
$\text{LiCl}$	0.2-0.5	2.5 (300%)	Graphite	Zr
$\text{LiCl}$ -0.5 wt.% $\text{Li}_2\text{O}$	0.5	1.5 (200%)	Graphite	Zr (M), $\text{Li}_2\text{ZrO}_3$ (m)
$\text{LiCl}$ -1 wt.% $\text{Li}_2\text{O}$	1.0	2.0 (250%)	Platinum	Zr (M), $\text{Li}_2\text{ZrO}_3$ (m)

M = Major, m = minor

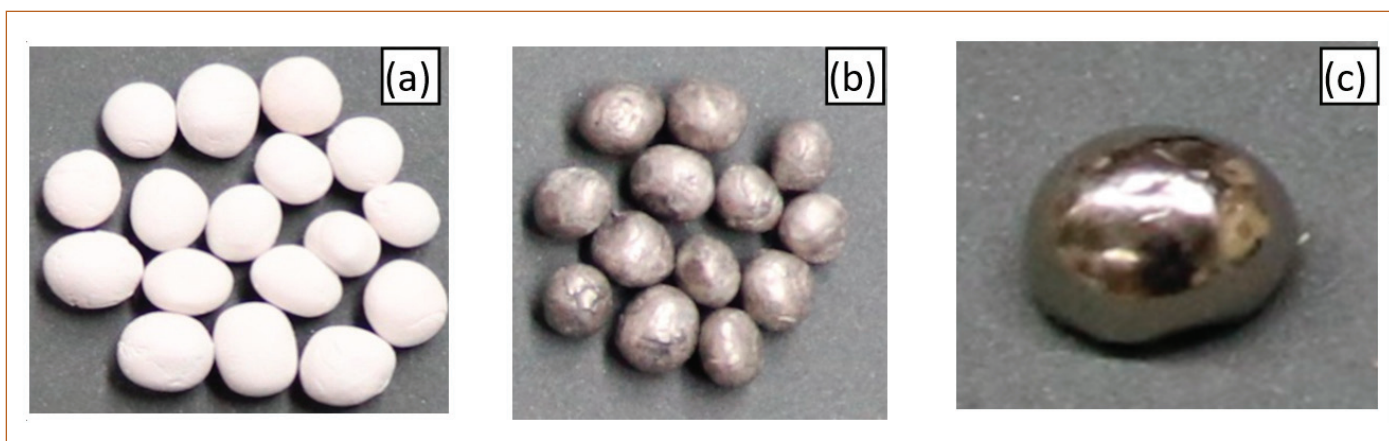


Figure 5: Photograph of  $\text{TiO}_2$  granules (a) before electrolysis (b) after electrolysis and (c) consolidated Ti button obtained by arc melting.

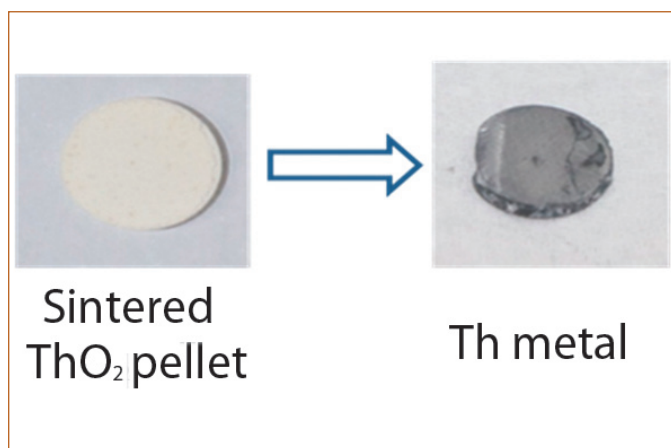


Figure 7: Photographs of sintered  $\text{ThO}_2$  pellet before and after electrochemical reduction

### Electro-reduction of $\text{TiO}_2$

Titanium is considered as a strategic metal due to its excellent properties including strength, corrosion-resistance and biocompatibility. Titanium is produced by the conventional Kroll process, where  $\text{TiO}_2$  is carbochlorinated at  $900^\circ\text{C}$  to  $\text{TiCl}_4$ , which is subsequently chemically reduced to titanium by magnesium. The batch process is labour-intensive and cumbersome and hence the cost of titanium is prohibitively expensive. Thus, there have been continuous efforts to improve the existing process or develop an alternative process for production of titanium. FFC Cambridge process is well suited for the reduction of  $\text{TiO}_2$  to Ti and hence being extensively studied for production of titanium all over the world. Some basic studies were carried out in our laboratory to understand the fundamental aspects of electro-reduction of  $\text{TiO}_2$  with powder compacted and sintered pellets as well as sintered powders.

Results of a typical 10 g scale electro-reduction experiment, carried out with sintered  $\text{TiO}_2$  granules are given below. Step-wise potential was applied (0.3 V increment) from 2.5 V to 3.1 V. The electrode was held (2.5 V for 10 h, 2.8 V for 24 h and 3.1 V for 10 h) at each voltage until the electrolytic current decreased to the lowest stable value. The outlet gas from the cell during the electrolysis period was tested for  $\text{CO}_2$  using barium hydroxide solution. De-oxidation reactions were continued until the absence of  $\text{CO}_2$  evolution (indicated by absence of white precipitate) on the anode at a given applied potential.  $\text{CO}_2$  monitoring was used to control the electrolysis. The granules after the run were washed by ultrasonating them with dilute HCl followed by distilled water to remove the adhered salt.

The photographs of the original granules and the product obtained after electrolysis are given in Figure 5a and 5b respectively. About 1 g of the Ti metal product was arc-melted to obtain a fine Ti button (Figure 5c). The oxygen content of the Ti metal button was estimated as 150 ppm by inert gas fusion technique.

### Electrochemical reduction of solid $\text{ThO}_2$ to Th

The conversion of  $\text{ThO}_2$  to Th is considered important for future metal fuelled fast nuclear reactors. Electrochemical deoxidation studies of  $\text{ThO}_2$  were carried out in both FFC Cambridge and electro-calciothermic methods in pure  $\text{CaCl}_2$  and  $\text{CaCl}_2$ -0.5wt.%  $\text{CaO}$  melts respectively. The results of the studies showed that thorium dioxide was converted to thorium in a single step without the formation of any intermediate compounds similar to the conversion of  $\text{UO}_2$  to U. It was observed that the reduction occurred much faster in the electro-calciothermic process than in the FFC process. The XRD of  $\text{ThO}_2$  pellet before and after electrolysis (Figure 6), confirmed the electrochemical deoxidation of  $\text{ThO}_2$ . Figure 7 shows the photographs of conversion of solid  $\text{ThO}_2$  pellet to Th metal.

Direct electrochemical conversion of solid metal oxides to metal is a single step high temperature molten salt electrolysis process that offers a vast advantage over conventional chemical and electrochemical methods for production of metal from corresponding oxides. This generic process can be used to prepare a number of metals in the periodic table, considering the chemical and electrical characteristics of the metal oxides and metal. R&D work on the metal production processes is being pursued for the past two decades, none is developed to a scale for commercial exploitation as of today, though significant strides have been made in the electrochemical reduction of  $\text{UO}_2$  and spent oxide fuels. The persistent efforts over a long period of time might lead to development of these processes for commercial exploitation in the years to come. The simplicity and the environment-friendly nature of the direct solid-state electro-deoxidation processes when compared to the cumbersome, labour-intensive and unsafe nature of conventional metal production processes, make a strong case for development of the former processes for metal production for the modern world.

*Reported by*

*R. Kumaresan and colleagues*

*Materials Chemistry & Metal Fuel Cycle Group*

## Development of Next Generation Instrumentation & Control Systems using Indigenous Real-Time Operating System for FBRs

Instrumentation and Control (I&C) systems provide protection, control, supervision and monitoring in Nuclear Power Plants (NPP). Some of these functions are safety critical, safety related and non-nuclear safety. NPP systems and equipment are classified (or categorized) depending on their relationship to plant safety. In general, a graded classification approach is adopted wherein the more direct relationship of a system to a safety function, the higher is its classification.. This ensures systematic application of appropriate design & engineering techniques thereby avoiding over-design. Extensive developmental activities have been taken up at Indira Gandhi Centre for Atomic Research (IGCAR) for the on-going research and power reactor programs and the critical facilities.

Indigenous activities in the development of I & C systems include monitoring and control electronics, special sensors & detectors and have paved the way to self-reliance in the fast reactor nuclear industry. Apart from ensuring functional requirements, design of electronics needs to meet high level of reliability, safety and security standards.

IGCAR has developed a large number of Instrumentation and Control (I&C) systems for various applications in PFBR like Distributed Digital Control Systems (DDCS) as shown in Figure 1. These embedded systems were developed without Real-time Operating System (RTOS), due to non-availability of indigenously

developed and certified RTOS. The Hindustan Aeronautics Limited (HAL), Bangalore has developed indigenous RTOS based on international standards such as Aeronautical Radio Incorporated (ARINC)-653 and provides the underlying system with absolute reliability, maximum real-time performance and enhanced security. The RTOS is also certified by Centre for Military Airworthiness and Certification (CEMILAC) for airborne applications.

A “Confidentiality Agreement” has been signed between IGCAR and HAL to jointly develop RTOS for IGCAR’s hardware platform for future FBRs. The use of HAL-RTOS will not only ensure real-time application execution in a fault-tolerant manner but also enhance the overall safety and security of the nuclear power plant.

### Benefits of RTOS

A Real-Time Operating System is a software that provides services and manages processor resources for applications in safety critical systems. These resources include processor cycles, memory, peripherals and interrupts. The main purpose of RTOS is to allocate processing time among various tasks of the embedded software and necessarily perform those tasks in time. This typically involves a division of the software into pieces, commonly called “tasks” or “threads” and creating a run-time environment that provides each thread with its own virtual microprocessor (“Multithreading”). Basically, a virtual microprocessor consists of a virtual set of microprocessor resources, e.g., register set, program counter, stack memory area and a stack pointer. While executing, a thread uses the physical microprocessor resources, but each thread retains its own copy of the contents of these resources as if they were its own private resources (the thread’s “context”).

The Real-Time Operating System controls thread execution and the accompanying management of each thread’s context. Each thread is given a priority by the designer, to control which thread should run if more than one is ready to run (i.e, not blocked). When a higher-priority thread (compared to the running thread) needs to execute, the RTOS saves the currently running thread’s context to memory and restores the context of the new thread. The process of swapping the context of threads is commonly called context switching.

This transfer of control to another thread is immediate and invisible to the embedded software. In fact, this invisibility might be the most fundamental benefit of an RTOS. Instead of embedding processor allocation logic inside the application software, it’s done by the RTOS. This arrangement isolates the

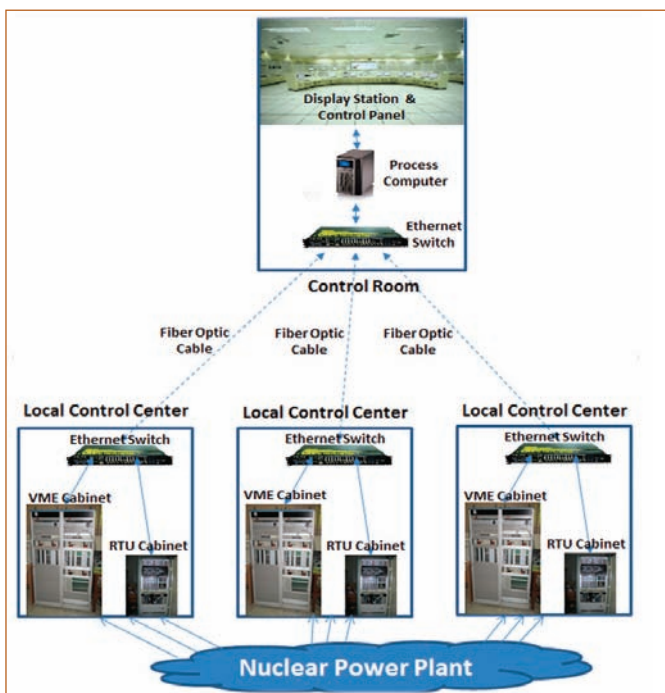


Figure 1: Distributed Digital Control Systems for PFBR

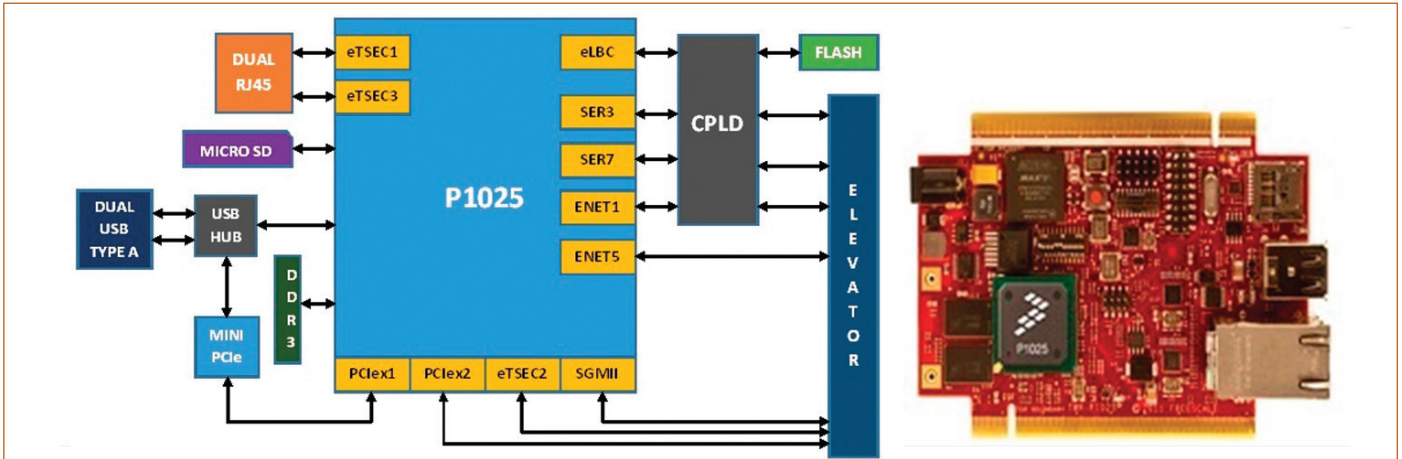


Figure 2: Block Diagram of P1025 Tower System and CPU Board

processor allocation logic and makes it much easier to predict and adjust the run-time behavior of the embedded device.

It's important to note that an RTOS offers pre-emption which is the action of switching to a higher-priority thread instantly and transparently, without having to wait for completion of the lower-priority thread. In addition to processor allocation, an RTOS also provides additional communication, synchronization and memory allocation services.

**Hardware platform for porting RTOS**

For rapid prototyping, it was decided to use P1025 tower module available from Freescale. The P1025 is a controller module featuring a dual core e500v2 based microprocessor in a 561 pin package with a maximum core operating frequency of 533 MHz. It can be used both in stand-alone or in the Freescale Tower System. The power supply required is 5V through barrel connector. The block diagram of P1025 tower system and CPU board is shown in Figure 2.

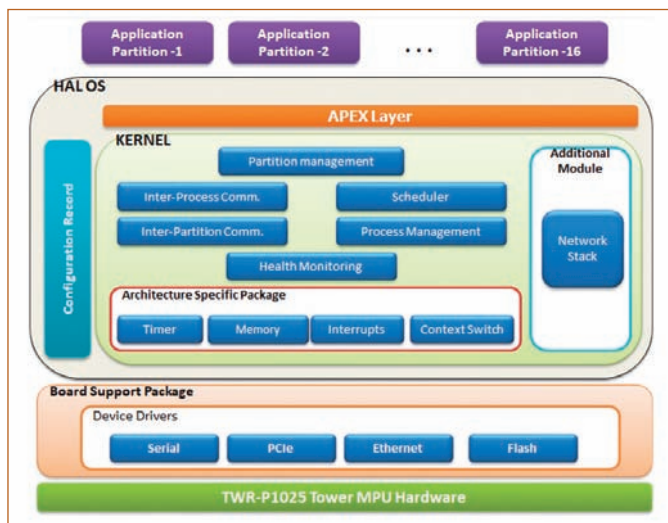


Figure 3: Architecture of HAL-RTOS

The P1025 Tower Module has the following features -Dual core P1025 in a 561 TEPBGA package operating up to 533 MHz, P1025 JTAG, CPLD JTAG, three axis accelerometer (MMA8451Q), two user-controllable LEDs, one reset pushbutton switch, ten-way DIP Switch for configuration, microSD card slot, mini-PCIe slot, two 10/100/1000 Mbps Ethernet RJ45, two USB2.0 type A, one mini-USB type B dual UART, 512 MB DDR3@667 MHz, 64 MB flash, IEEE 1588 pinned to header with DAC and VXCO.

**HAL-RTOS Kernel**

HAL-RTOS is a safe and reliable space and time partitioned real-time operating system intended for use across real time embedded platforms. It is based on avionics application software standard interface ARINC 653, Part 1. The overall architecture of HAL-RTOS is shown in Figure 3.

**RTOS Build structure**

The build structure of RTOS folder is shown in Figure 4. It contains following sub-folders:

**Kernel:** This folder contains kernel's header files to be used by board support package and system integration hooks.

**XML\_Parser:** This folder contains host based XML configuration utility. This software runs on the host system to read and validate configuration data supplied by system integrator in XML configuration files.

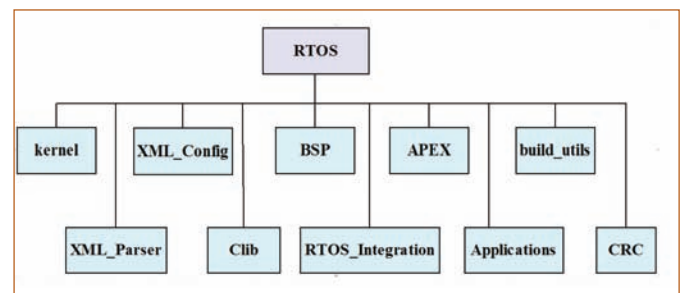


Figure 4: RTOS Build Structure

**XML\_Config:** This folder contains the XML configuration files and corresponding XML schemas. Following Configuration files shall be provided by the system integrator as an input to the XML Configuration Utility: KernelConfig.xml, MemoryConfig.xml, PartitionConfig.xml, PartitionScheduleConfig.xml, HMConfig.xml, FileSystemConfig.xml, NetworkStackConfig.xml & ModuleConfig.xml.

**CLib:** This folder contains the ANSI-C library header files. These headers files may be used in board support package and hook files.

**BSP:** This folder has a sub-folder for each board supported by RTOS. These board specific folders have source code for board support package and device drivers for the board. The folder also contains a header file BoardInterface.h. This file is common for all boards supported by RTOS. It contains the prototypes for interface functions, which are implemented by a board support package to be compatible with HAL-RTOS.

**RTOS\_Integration:** This folder contains an integration project to link kernel, C library, BSP and hooks to create RTOS image file and hooks for system integrator to add kernel code.

**Apex:** This folder contains the header files for APEX interface for applications. These functions are system calls available to application code for requesting service from kernel.

**Applications:** This folder is the root location for all applications/partitions. Each subfolder in “Applications” contains source code for one partition.

**build\_utils:** This folder contains utility files used while building the application image. File “PayloadValidation.c” compiled and executed after application image is created. It checks that the application image file not larger than the size specified for the same in XML configuration utility.

**Cyclic Redundancy Check (CRC):** This folder contains program for generating and adding checksum to application images and

configuration data. This program is executed on host as part of build process.

**Memory initialization and management**

The HAL-RTOS creates virtual address space with supervisor privilege, separate virtual address spaces for partitions with user privilege, no unauthorized access of Kernel memory region by partitions, no direct user access to Partition’s Object pools and Stack Overflow protection.

**API Library**

The API library lies in the user’s address space along with application code. When a kernel service is needed, the application process calls the API with the required parameters. The API validates the passed input parameters and returns error code if the parameters are not valid. If parameters are valid, it invokes corresponding kernel service routine. After completion of the requested service, the result is returned to the application process. The API library description is divided into several major categories like Partition Management services, Inter-partition communication services, Process Management services, Inter-process communication services, Health Management services and Time Management services.

**Partition management services:** The HAL-RTOS provides Partition Management service to allow users to run multiple file systems on the same device. The following APEX APIs are available: GET\_PARTITION\_STATUS & SET\_PARTITION\_MODE.

**Inter-Partition Communication:** In order to decouple the real-time operating system platform from the application software, HAL-RTOS defines an API called APplication EXecutive (APEX). Application software calls a partition and has its own memory space. It also has a dedicated time slot allocated by the APEX API. Within each partition, multitasking is allowed. The APEX API provides services to manage partitions, processes and timing, as well as partition/process communication and error handling.

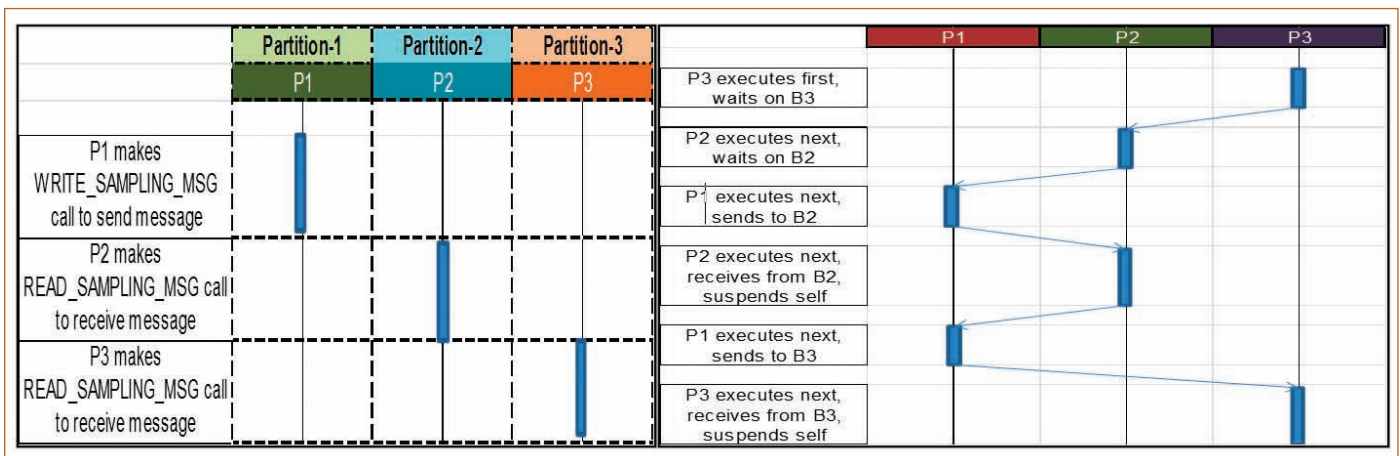


Figure 5: Inter-Partition & Inter-Process Communication

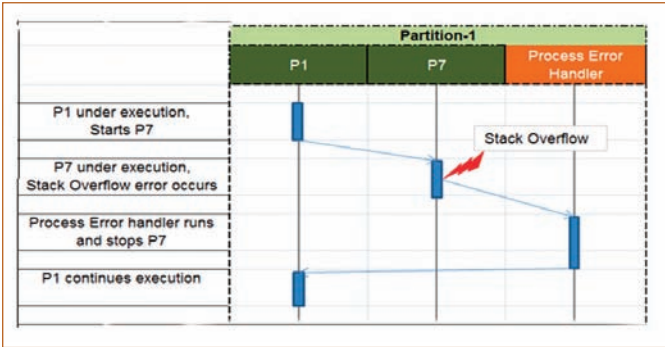


Figure 6: Health Management Services

- Partition-1: Process P6; Source Port – SP1
- Partition-2: Process P1; Destination Port – DP2
- Partition-3: Process P1; Destination Port – DP3
- Message transfer from SP1 to DP2 and DP3

**Process Management Services:** The HAL-RTOS allocates resources to processes, enable processes to share and exchange information, protect the resources of each process from other processes and enable synchronization among the processes. The following APEX APIs are available in HAL-RTOS: GET\_PROCESS\_ID, GET\_PROCESS\_STATUS, CREATE\_PROCESS, SET\_PRIORITY, SUSPEND SELF, SUSPEND, RESUME, STOP SELF, STOP, START, DELAYED START, LOCK PRE-EMPTION, UNLOCK PRE-EMPTION & GET MY ID.

**Inter-Process Communication:** Inter-process communication (IPC) is a mechanism, which allows processes to communicate with each other and synchronize their actions. The communication between these processes can be seen as a method of co-operation between them. Processes can communicate with each other through both shared memory & message passing is shown in Figure 5.

- Processes– P1, P2, P3 with priority P3>P2>P1
- Message Buffer B2 and B3

**Health Management Services:** It monitors process error and stack overflow error as shown in Figure 6.

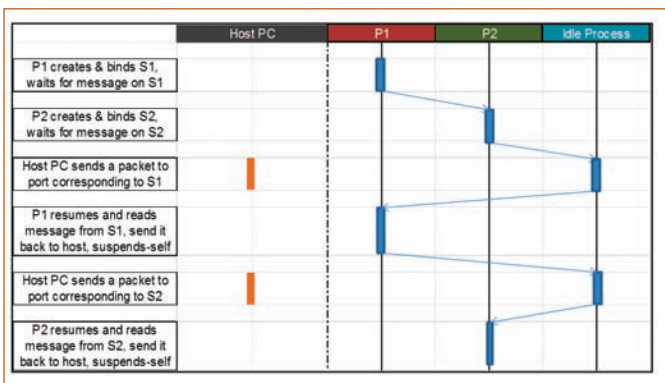


Figure 7: Communication between Host PC & Target System



Figure 8: Handing Over Ceremony at Defence Expo - 2020, Lucknow

**Time Management Services:** Functions are provided for system clock setting & reference and for referencing system operating time as follows: TIMED\_WAIT & PERIODIC\_WAIT & GET\_TIME.

**Additional API**

**Mutex** is a mutual exclusion object that synchronizes access to a resource. It is created with a unique name at the start of a program. The Mutex is a locking mechanism that makes sure, only one thread can acquire the Mutex at a time and enter the critical section as per following APIs: CREATE\_MUTEX, GET\_MUTEX\_ID, WAIT\_MUTEX, SIGNAL\_MUTEX, GET\_MUTEX\_STATUS, GET\_MUTEX\_ID. APIs for I/O management are as follows: OPEN, READ, WRITE, IOCTL & CLOSE.

**Network stack API**

The network interface allows the network stack using UDP protocol to be transplanted into an operating system, as it provides a common interface between Host PC and the target system OS kernel as shown in Figure 7. The following additional APIs are provided: socket, bind, connect, sendto, recvfrom, send, sendmsg, recv, recvmsg, setsockopt, getsockopt, shutdown, getpeername & getsockname.

- 2 Processes– P1 and P2, with priority P1>P2
- 2 Sockets– S1 (Port: 50000) and S2 (Port: 55000)
- Host PC IP: 192.168.1.2, Target System IP: 192.168.1.3

HAL-RTOS has been successfully ported on to IGCAR’s hardware platform. In recent Defence Expo-2020 in Lucknow, the Hindustan Aeronautics Limited handed over documents related to India’s first indigenously designed and developed RTOS to IGCAR, Kalpakkam. The document was handed over by Mr Arup Chatterjee, Director (Engineering and R&D), HAL to Ms T. Jayanthi, Director (Electronics & Instrumentation Group), IGCAR in the presence of Mr R. Madhavan, HAL CMD and other senior officials from HAL and IGCAR (Figure 8).

Reported By  
T. Jayanthi & Colleagues  
Electronics & Instrumentation Group

## Young Officer's FORUM



Shri D. Nanda Gopala Krishna has been working as a Scientific Officer at the Corrosion Science and Technology Division, Indira Gandhi Centre for Atomic Research since July 2010. He acquired B.Sc. and M.Sc. (Physics) degrees from the University of Mysore, in 2007 and University of Hyderabad in 2009, respectively. He registered for PhD with HBNI under the guidance of Dr. John Philip in 2017. His research interests include X-ray photoelectron Spectroscopy (XPS) valence band analysis for the identification of material surface phase composition at nano-scale. He has authored/co-authored 47 peer reviewed research articles in international journals.

### Enhanced Corrosion Resistance and Photocatalytic Activity of Thermally Oxidized Titanium: Role of Titania Film Thickness, Topography and Phase Composition

Titanium (CP-Ti) and its alloys exhibit exceptional corrosion resistance in a wide range of environments and are known for their high specific strength, biocompatibility and non toxicity.

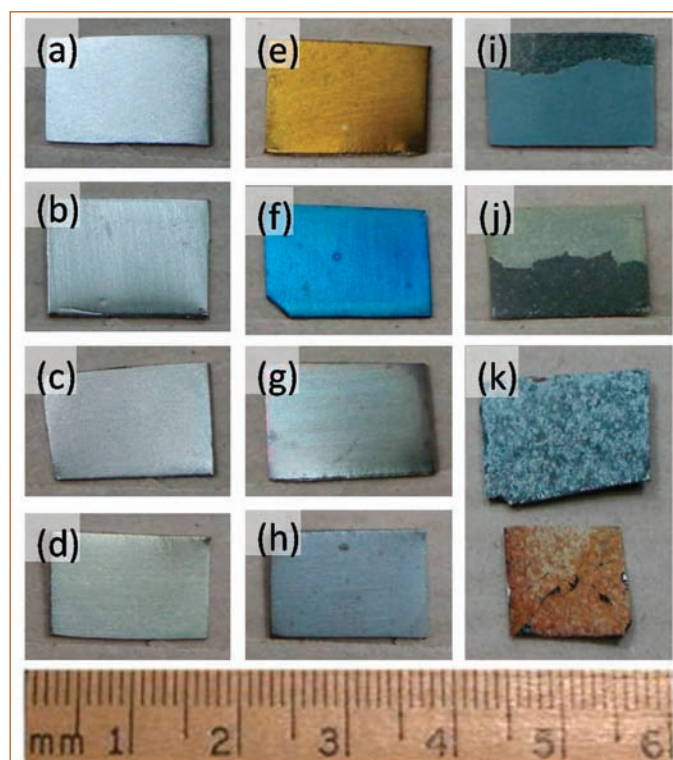


Figure 1: Photographs of the CP-Ti specimens air oxidized at different temperatures for 1 h showing a thickness dependant colour variation of the oxide layers formed. (a) 25°C (room temperature), (b) 100 °C, (c) 200 °C, (d) 300 °C, (e) 400 °C, (f) 500 °C, (g) 600 °C, (h) 700 °C, (i) 800 °C (partial peeled-off oxide layer), (j) 900 °C (partial peeled-off oxide layer) and (k) 1000 °C: Top - titanium substrate without and (Below) with titania layer

The chemical inertness of these materials is attributed to the continuous titania ( $\text{TiO}_2$ ) film formed on the surface that acts as a barrier between the metal and the electrolyte medium thus preventing corrosion.  $\text{TiO}_2$  films formed by thermal oxidation have a higher corrosion and wear resistance because of dense, uniform, compact and crystalline nature than the films formed by anodization, which are porous, rough and amorphous. For biomedical application, the corrosion resistance of an implanting material is the prime factor that determines its service life in the host body. Although CP-Ti and its alloys are preferred materials for biomedical applications owing to their superior material properties, CP-Ti is not inherently anti-bacterial and the risk of infection due to the implant failure gives rise to health complications. This study was aimed at developing CP-Ti with better antibacterial properties and understanding the role of surface morphology, crystallinity and thickness of the nanoscale film grown by thermal oxidation.

The CP-Ti grade 2 metal specimens, when air oxidized for 1 h at different temperatures in muffle furnace, display different colours due to the growth of titania ( $\text{TiO}_2$ ) layers of different thickness over its surface as shown in Figure 1. The colour of the  $\text{TiO}_2$  layer is correlated with its thickness following the principle of thin film interference. The oxide films formed at above 700°C were not adherent to the CP-Ti substrate.

X-ray photoelectron spectroscopy (XPS) is used to characterize the chemical and phase composition of the oxide films formed over thermally oxidized CP-Ti specimens, by core level and valence band analysis, respectively. The survey spectrum of all the oxide films show the presence of elements of titanium (Ti 2p @ 460 eV), oxygen (O 1s @ 530 eV) and carbon (C 1s @

285 eV) whose concentration (at-%) across the specimens were observed in the range as  $20 \pm 1$  :  $46 \pm 1$  :  $34 \pm 2$ , respectively. The Ti 2p core level region for the oxide layers indicates the layers are made of TiO<sub>2</sub>. The films grown at temperatures at or below 200 °C showed sub-stoichiometric oxides (Ti<sub>2</sub>O<sub>3</sub>, TiO and Ti<sub>2</sub>O) at the TiO<sub>2</sub>-metal interface. The O 1s core level region for the oxide layers suggest the presence of -O-Ti-, -C-O- and -OH bonds but the films grown at temperatures at or below 100 °C showed the presence of adsorbed moisture (H<sub>2</sub>O) on their surface.

To determine the surface phase composition of the TiO<sub>2</sub> films on CP-Ti metal specimens, the valence band region (0–13 eV) of the samples was analyzed as shown in Figure 2. The region is spanned by the O 2p and Ti 3d density of states. The valence band data of the oxide layers, formed over the CP-Ti metal, at temperature below 200 °C is broadly divided into two regions: 0–3 and 3–10 eV. The valence band in the 3–10 eV region correspond to mainly O 2p character (5.5 eV) along with the O 2p-Ti 3d hybridized states (7.5 eV) of the oxide layer while the 0–3 eV region correspond to the metallic Ti 3d character of the

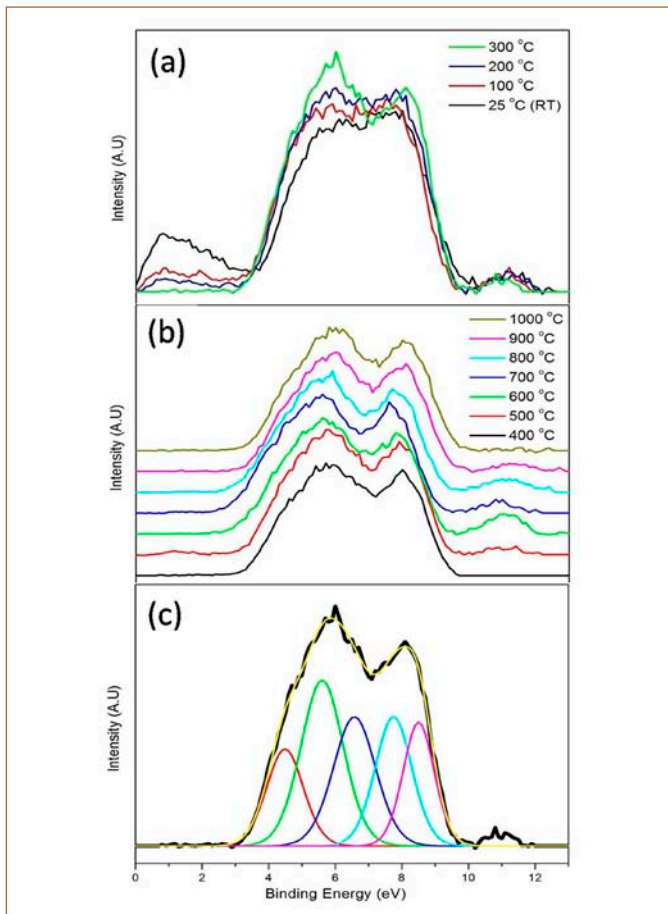


Figure 2: Comparison of the XPS valence band data of the oxide layers formed over cp-Ti specimens air oxidized for 1 h at different temperatures: (a) 25 to 300 °C, (b) 400 to 1000 °C and (c) deconvoluted valence band representing the oxidized specimen above 300 °C

sub-stoichiometric oxides at the interface and the metallic Ti substrate below. The 3–10 eV region with a single broad peak structure correspond to the amorphous phase of titania. Above 300 °C, only the 3–10 eV region was observed since the oxide layer making up the entire probing depth of XPS is composed of only TiO<sub>2</sub> as was observed with the Ti 2p core level. However, the peak structure of the valence band region showed two-peak structure at 5.5 and 7.5 eV. The higher binding energy peak area (%) of the valence band was calculated for all the specimens oxidized above 300 °C, by deconvoluting the valence band into five peaks, and found to be at  $35.0 \pm 0.65$  which is identical as calculated for rutile phase nanopowder at  $35.0 \pm 0.35$ .

Thus, the valence band analysis showed that the titania layers formed over CP-Ti is amorphous up to an oxidizing temperature of 200 °C while the layers formed above 300 °C are rutile phase and the transformation here occur directly without the formation of a metastable anatase phase at intermediate temperatures.

The thickness of the films for the titanium specimens oxidized up to 200 °C is calculated, assuming a homogeneous film for simplification, using Beer-Lambert's law for the electron propagation through the material surface:

$$d_{\text{ox}} = \lambda_{\text{ox}} \sin \theta \ln \left[ \frac{N_{\text{m}} \lambda_{\text{m}} I_{\text{ox}}}{N_{\text{ox}} \lambda_{\text{ox}} I_{\text{m}}} + 1 \right] \quad (1)$$

Here  $d_{\text{ox}}$  is the oxide film thickness,  $\theta$  is the take-off angle of the photoelectron,  $I_{\text{ox}}$  and  $I_{\text{m}}$  are the area percentages of the oxide and metal peaks from the high-resolution spectrum,  $\lambda_{\text{m}}$  and  $\lambda_{\text{ox}}$  are the IMFP and  $N_{\text{m}}$  and  $N_{\text{ox}}$  are the volume densities of the metal atoms in the metal and oxide, respectively. While those films formed at above 300 °C were quantified by Ar<sup>+</sup> ion sputtering and evaluating the oxygen to Ti ratio (O:Ti). The sputtering is carried out until the O:Ti ratio gets saturated. It is observed that the saturation value of the ratio increased from 0.3 for the CP-Ti metal sample oxidized at 200 °C to 0.6 for the sample oxidized at 700 °C, which suggests that the amount of dissolved oxygen within the metal sub-surface increases with increasing temperature. However, the O:Ti ratio of all the specimens at their surfaces, excluding the contribution from adventitious carbon contamination layer in the form -C-O-, were identical at  $2 \pm 0.05$ , suggesting that the oxide layer is TiO<sub>2</sub>. To evaluate the relative thickness of the oxide films, the sputter time taken to reach a O:Ti ratio of 1 was chosen for all the specimens. The thickness of the oxide layer formed over CP-Ti at 200 °C was evaluated based on the relative concentration of oxidic to metallic Ti 2p core level peaks and found out as 6 nm (TiO<sub>2</sub> + Ti<sub>2</sub>O<sub>3</sub> / O:Ti > 1), apart from 1 nm thick sub-stoichiometric oxide layer (TiO + Ti<sub>2</sub>O / O:Ti ≤ 1) at the oxide-metal interface. The calculated sputter rate of the oxide layer was 4.3 nm.min<sup>-1</sup>, based on which the thickness of the oxide films grown from 300 to 700 °C are given in the Table 1.

Table 1: Comparison of the thickness of oxide films formed over CP-Ti after thermal oxidation in air at different temperatures for 1 h as evaluated by XPS depth profile

Specimen Oxidation Temperature / °C	Film thickness / nm
25 (RT)	3±0.2
100	5±0.3
200	6±0.4
300	11±1
400	16±1
500	32±2
600	85±5
700	540±30

The corrosion performance of different oxidized CP-Ti is studied in simulated body fluid (Ringer's solution) using potentiodynamic polarisation and electrochemical impedance spectroscopy techniques and the underlying mechanism of improved corrosion is obtained. The anodic polarization of different oxide films in the Ringer's solution is shown in the Figure 3. The passive current ( $i_{pass}$ ) and the passive range, up to 1.5 V, of the amorphous oxide films grown up to 200 °C decreased with increase in oxidation temperature as a result of increased film thickness. The rutile film specimens, formed at and above 300 °C, showed a lower  $i_{pass}$  value as compared to the amorphous ones. In the case of amorphous films, the rate of anodic reaction increases linearly from their respective corrosion potentials ( $E_{corr}$ ), before reaching the passive range. Also, the potential range of the linear region increased from 0.3 to 0.5 V above the  $E_{corr}$  as the growth temperature increased from room temperature

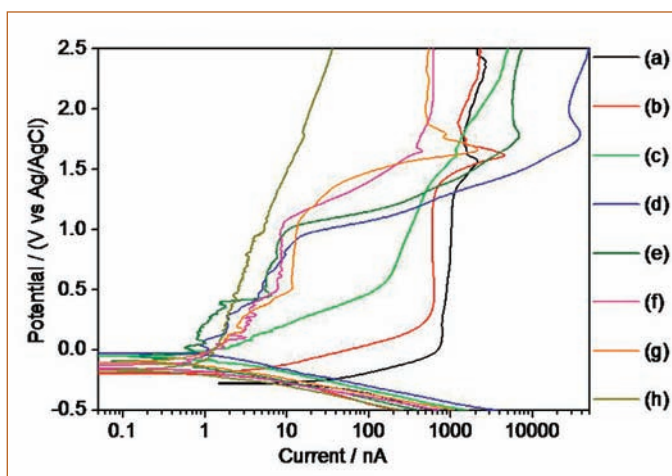


Figure 3: Comparison of the potentiodynamic anodic polarization curves in Ringer solution at room temperature for the Ti oxide layers grown for 1 h at various temperatures: (a) room temperature (25-30 °C), (b) 100, (c) 200, (d) 300 (e) 400, (f) 500 (g) 600 and (h) 700 °C

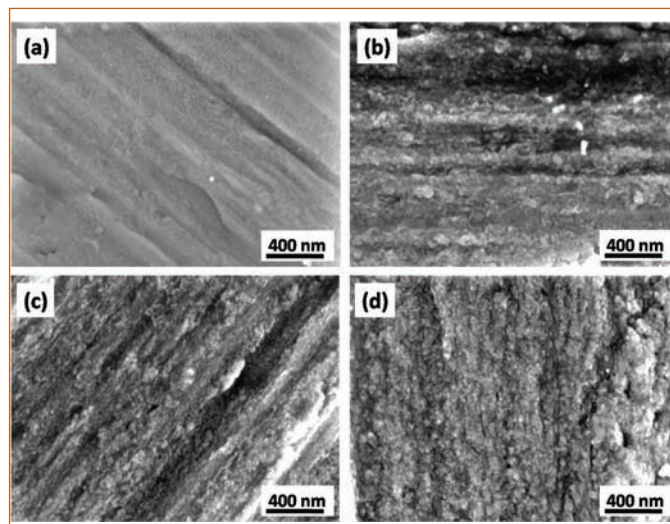


Figure 4: Surface morphology of the oxide layers formed over CP-Ti oxidized for 1 h at (a) 400, (b) 500, (c) 600 and (d) 700 °C imaged by FESEM at 50 kV

to 200 °C. However, in the case of the crystalline films, the region of passivity is seen right from their respective  $E_{corr}$  values. The amorphous films showed trans-passivity between 1.5 to 1.65 V and secondary passivation behaviour above 1.65 V, while the rutile films showed a trans-passivity for a much broader range (1.0 to 1.7 V) except for the grown at 700 °C sample, which did not show any trans-passivity behaviour. However, variation in the current densities within the trans-passive region was 2 to 3 orders of magnitude higher in the case of the crystalline films as compared to the amorphous films, where the change was less prominent with less than an order of magnitude change. This suggests that the rutile phase is more corrosion resistant in chloride medium at lower anodic potentials (< 1 V) and higher film thickness (> 100 nm).

The polarization resistance,  $R_p$ , of the oxide films at their respective  $E_{corr}$  values were also calculated following the Tafel equation:

$$R_p = [(b_a b_c)] / [2.303(b_a + b_c) i_{corr}] \quad (2)$$

Here,  $b_a$  and  $b_c$  are the anodic and cathodic Tafel constants (slopes), respectively and  $i_{corr}$  is the corrosion current obtained from the polarization curves of Figure 3. The variation of polarization resistance,  $R_p$  values (Table 2) revealed that the  $R_p$  reaches a peak value  $\sim 10^8 \Omega \cdot \text{cm}^2$  for the oxide layer grown at 400 °C ( $\sim 10^6 \Omega \cdot \text{cm}^2$  for the native oxide layer). The  $R_p$  value decreased to  $\sim 10^7 \Omega \cdot \text{cm}^2$  for the specimens oxidized at 500 to 700 °C despite a significant increase in the thickness of the oxide layer. The sudden increase in the roughness of the oxide layers (Figure 4) at 500 to 700 °C results in an increase of true surface area of the specimen as compared to its geometric area. Consequently, the total surface charge transfer reaction at the electrolyte-oxide surface interface increases, leading to a reduction in the  $R_p$  value.

Thus, the highest  $R_p$  value observed for the titania film grown at the oxidation temperature of 400 °C for 1 h could be due to the optimal surface roughness and film thickness.

The impedance data of the different oxide layers, modelled with equivalent circuits, revealed the nature of oxide layers and their interaction with the electrolyte. The films formed up to a temperature of 400 °C showed two time constants while those formed at 500 to 700 °C showed three constants (Figure 5). The dual layer structure of the oxide layer observed for the lower temperature ( $\leq 400$  °C) specimens has an outer barrier titania layer and an inner sub-stoichiometric oxide layer. For the oxide films grown at 500 to 700 °C, the presence of an additional time constant could be accounted for the change in the surface morphology as shown in the Figure 4.

Table 2: The corrosion parameters calculated for the different Ti oxide layers in Ringer solution from the anodic polarization curves of Figure 3 by Tafel analysis

Specimen Oxidation Temperature / °C	Polarization resistance ( $R_p$ ) / $M\Omega.cm^2$
25 (RT)	$1.0 \pm 0.2$
100	$9.0 \pm 1.0$
200	$39 \pm 4$
300	$56 \pm 4$
400	$90 \pm 13$
500	$65 \pm 4$
600	$52 \pm 5$
700	$54 \pm 3$

The photocatalytic activity of  $TiO_2$  films formed on the CP-Ti surface by thermal oxidation was assessed by evaluating the degradation of methylene blue (2 mol/m<sup>3</sup> MB) solution under visible light exposure for 4 h. The absorbance values of MB solution after 4 h exposure with different Ti specimens are shown in Figure 6. The absorbance values for all the specimens were about 1.1, except for the one oxidized at 400 °C, which showed a value of  $0.83 \pm 0.03$ , indicating the significant photocatalytic activity.

Reflectance spectroscopy has been carried out to understand the photocatalytic activities of thermally oxidized CP-Ti and is shown in Figure 7a, which revealed that the reflectance is < 1 % (absorption > 99 %) at 410 nm for the oxide film of 15 nm thick grown at 400 °C. The energy of absorption peak in the blue wavelength is 3.0 eV, which also corresponds to the band gap of rutile titania.

The relation between the photon wavelength,  $\lambda$  and its energy, E, is as follows:

$$E = hc/\lambda \tag{3}$$

Here, h is the Planck constant ( $4.136 \times 10^{-15}$  eV.s), c is the speed of light in vacuum ( $2.998 \times 10^8$  m.s<sup>-1</sup>). The absorption of light

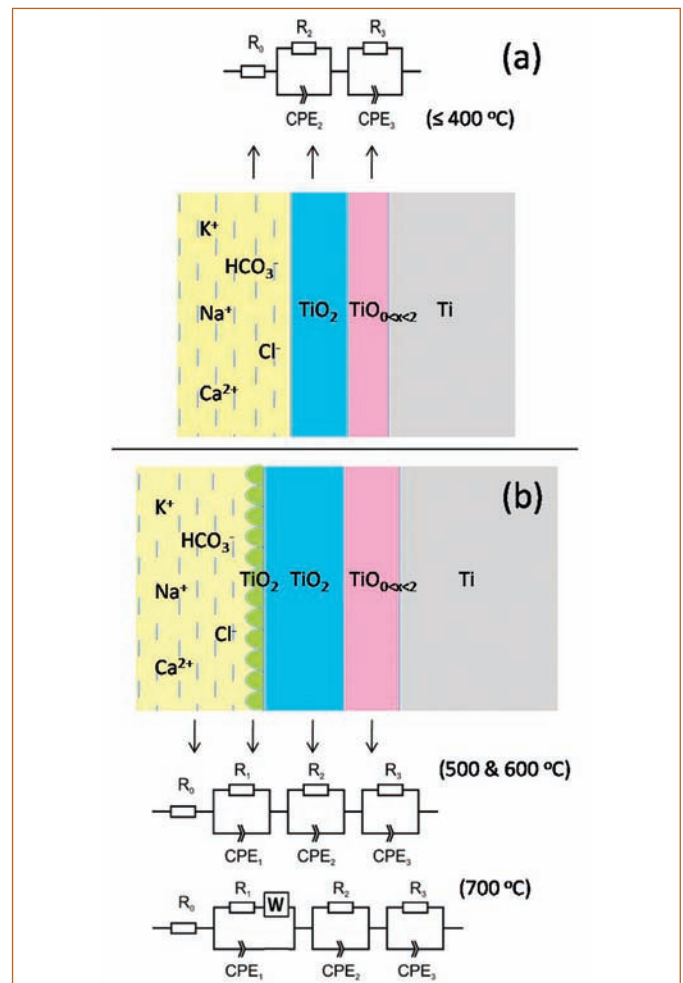


Figure 5: Schematic showing the different equivalent circuits used to fit the impedance curves and to model the oxide layers formed over CP-Ti at lower, (a)  $\leq 400$  °C and higher, (b)  $\geq 500$  °C temperature ranges

matching the band gap leads to the excitation of the valence electrons to the conduction band, along with the creation of holes in the valence band. Thus, the higher absorption of the blue light by the rutile film grown at 400 °C results in the increased e-h

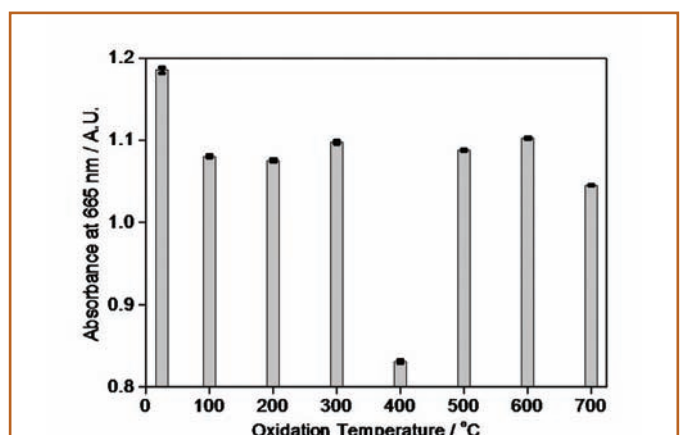


Figure 6: Comparison of the absorbance values of the methyl blue solution at 665 nm wavelength light for the oxidized CP-Ti specimens after 4 h exposure to visible light

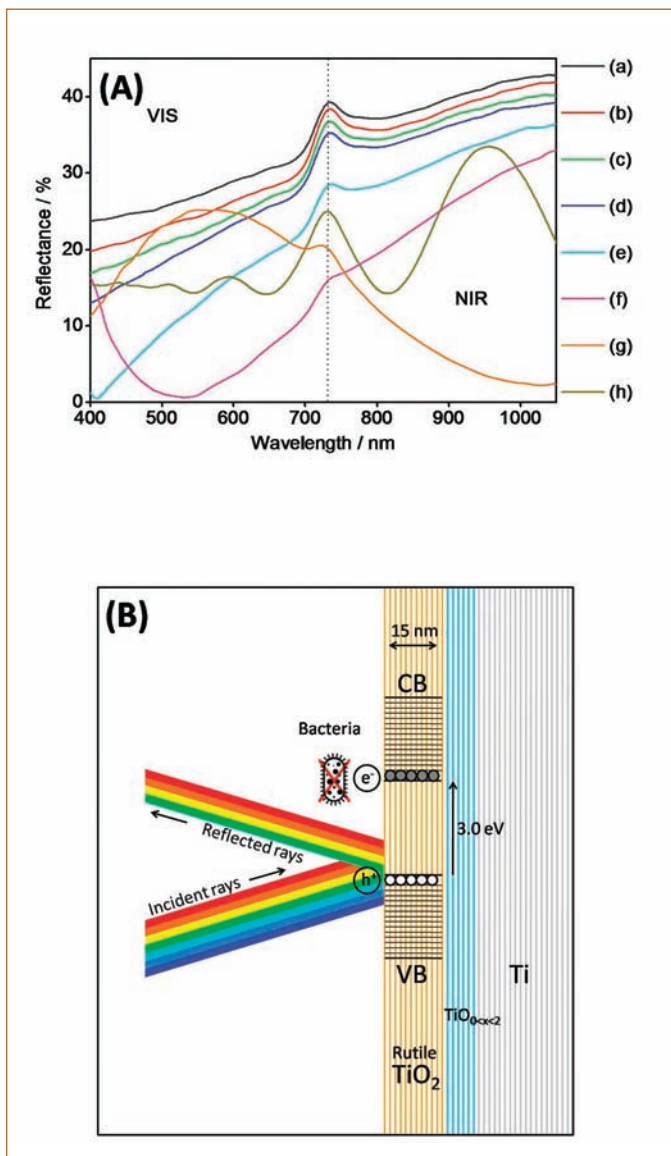


Figure 7: (A) Comparison of the reflectance from the oxide layers formed over the CP-Ti specimens oxidized for 1 h at (a) room temperature (25-30 °C), (b) 100, (c) 200, (d) 300 (e) 400, (f) 500 (g) 600 and (h) 700 °C. (B) Schematic showing the preferential absorption of ~410 nm wavelength light (~ 3 eV) of the rutile titania thin film grown to ~15 nm thick over metallic Ti substrate by thermal oxidation enhancing its photocatalytic activity and thus its antibacterial property

recombination time and thus the increased photocatalytic activity. An enhanced number of electron-hole (e-h) pairs generation within the film is also possible due to the efficient absorption of the light at ~ 410 nm wavelength. This phenomenon is shown schematically in the Figure 7b. This implied that the thin film interference phenomenon improves the photocatalytic activity of the rutile phase titania films at ~ 15 nm thickness. Thus, the thermal oxidation parameters of 400 °C and 1 h in ambient atmosphere are considered as an ideal condition for obtaining the maximum corrosion resistance and photocatalytic activity.

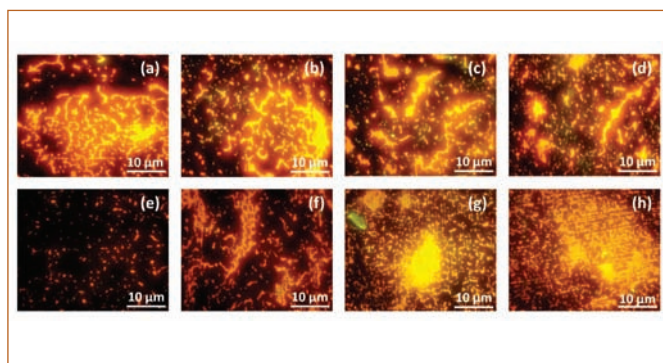


Figure 8: Epifluorescence micrographs of the biofilms of *Pseudomonas sp* attached on the CP-Ti specimens thermally oxidized for 1 h at (a) room temperature (25-30 °C), (b) 100, (c) 200, (d) 300 (e) 400, (f) 500 (g) 600 and (h) 700 °C exposed to visible light for 4 h

For evaluating the antimicrobial property of thermally oxidized CP-Ti specimens, a gram-negative bacterium, *Pseudomonas sp.* that was cultured in sterilized R2A medium for 16 h, was used. Epifluorescence micrographs of *Pseudomonas sp.* biofilms attached onto different CP-Ti specimens under illumination are shown in Figure 8. CP-Ti thermally oxidized at 400 °C showed the least density of bacterial cells, indicating the highest antibacterial activity, while the rest of all had a similar amount of attachment. The biofilms under darkness also showed a similar trend. On comparing the bacterial cells under both conditions, it was found that the decrease in density of attached cells was the maximum under illumination for the Ti sample oxidized at 400 °C. This indicates the dominant role of photocatalytic activity of the oxide layer is reducing the bacterial cell attachment. The least attachment of bacterial cells on the Ti surface thermally oxidized at 400 °C even under dark conditions suggests the role of polarization resistance of the oxide film in the antibacterial activity due to the electrochemical interaction between the bio-film and the substrate metal. An increase in the  $R_p$  value of film suppresses the electron transfer rate and thus the overall electrochemical reaction between the biofilm and substrate, thereby reducing the microbial growth.

This study confirms an anomalous enhancement of corrosion resistance and antibacterial property of CP-Ti surface in the presence of a uniform ~ 15 nm thick rutile titania film, formed by the thermal oxidation of CP-Ti at 400 °C for 1 h. It is understood that the selective absorption of light (410 nm), due to matching photon energy with the film band gap, drastically enhanced the photocatalytic activity and thus the antibacterial property of the CP-Ti. The corrosion resistance of the rutile phase titania films is found to be better than the amorphous films and strongly dependent on the film thickness and surface morphology. The impedance data accounts well for the dual layer structure with an outer barrier titania and inner substoichiometric oxide layer.

## Young Researcher's Forum



Dr. Raktima Basu obtained her M. Sc degree in Physics with the specialization of Radio Physics and Electronics from University of Burdwan, West Bengal in the year 2014. She joined IGCAR as a research scholar in the year 2015 and carried out her research work in Surface and Nanoscience Division.

She completed her Ph.D. dissertation in Physical Sciences from Homi Bhabha National Institute. Her doctoral research work is mainly focused on the understanding of the mechanism of phase transition in vanadium oxides and its application in various advanced technologies. Her current research interest is to explore the light-matter interaction using plasmonics.

## First Observation of Spin Wave in Vanadium dioxide

$\text{VO}_2$ , one of the most studied examples of a transition metal oxide, undergoes a metal-to-insulator transition (MIT) at 340 K. The near-ambient MIT makes  $\text{VO}_2$  a promising switchable material for oxide electronics, But the involvement of structural phase transition (SPT) makes it critical for device applications. The phase transition in  $\text{VO}_2$  is complex for its remarkable feature being to exhibit lattice, electronic and magnetic aspects.

As MIT is associated with SPT, a long-standing debate exists on whether the MIT is Mott driven or structure driven. During the structural transition from the low-temperature M1 (monoclinic;  $P2_1/C$ ) to R (tetragonal;  $P4_2/mnm$ ) at high temperature,  $\text{VO}_2$  undergoes intermediate phase changes such as M2 (monoclinic;  $C2/m$ ) and T (triclinic;  $C\bar{1}$ ). The M1 structure has the V-V pairs along  $a_{M1} \leftrightarrow 2C_R$  axis with alternate V-V separations of 2.65 Å (bonding) and 3.12 Å (anti-bonding). The M2 phase, in one sub-lattice, has the V-V pairs with alternate V-V separations of 2.53 Å (bonding) and 3.25 Å (anti-bonding) and V-V separation of 2.93 Å in another sub-lattice along  $b_{M2} \leftrightarrow 2C_R$  axis. The high-temperature tetragonal phase has the V-V separations of 2.87 Å. The triclinic T phase arises between M1 and M2. The interplay between the structural phases in  $\text{VO}_2$  is reported to be affected by the strain caused by external stimuli or by doping and defects.

The observation of low-frequency Raman modes ( $\sim 50$  to  $140 \text{ cm}^{-1}$ ) in the  $\text{V}_{1-x}\text{Mg}_x\text{O}_2$  systems stabilised in M1, T and M2 phases of  $\text{VO}_2$  are reported. It is argued that the strain due to Mg doping leads to the stabilization of M2 and T phases in the  $\text{V}_{1-x}\text{Mg}_x\text{O}_2$  system.

The low-frequency modes are found out to be originated due to the dimerized spins and are compared with the spinon vibrations calculated by considering perturbation due to spin-lattice coupling. Polarized Raman spectroscopy helps in finding the crystalline phase and crystallographic orientation of the samples as well as in understanding the lattice dynamics by finding the mode symmetries. As spinon vibrates independently from the holons (spin-charge separation), the orthogonal dependency of the phonon and spinon vibration in the polarized Raman study helps in finding the origin of the low-frequency Raman modes as spin waves. The observation and perceptiveness of spin-wave may help in finding new insight into the phase transition in  $\text{VO}_2$ .

$\text{V}_{1-x}\text{Mg}_x\text{O}_2$  nano- and micro-structures were grown by vapour transport process on high pure (99.99%) alumina boat using mixed  $\text{VO}_2$  powder and Mg powder (Sigma-Aldrich, 99%) as the source and Ar (99.9%) as the carrier gas. Substrates were kept at 10 mm away from the source parallel to the stream of carrier gas. The synthesis was carried out at 1100 K for 3 h. The concentration of the Mg dopant was controlled by changing the flow rate of the carrier gas. The synthesis was carried with the optimized flow of Ar (99.9%), e.g., 20, 40, 60, 80 and 100 sccm (samples, S2, S3, S4, S5 and S6, respectively) in the presence of Mg powder. Sample S1 was prepared with the flow of 20 sccm Ar, keeping other growth conditions same except the Mg powder. The structural properties of the as-grown samples were studied using synchrotron x-ray diffraction (XRD), installed at Indus-2 synchrotron facility (BL-11) at Ramanna Centre for Advanced

Technology (RRCAT), India, with a wavelength of 0.76089 Å and a Si(111) channel-cut monochromator. The vibrational modes of the synthesized samples were studied using a micro-Raman spectrometer (in Via, Renishaw, UK). The Raman signals were recorded using 514.5 nm excitation with an integration time of 20 s. The back scattered signals were dispersed with 1800 gr.mm<sup>-1</sup> grating and were recorded with a thermoelectrically cooled CCD detector. In order to perform polarized Raman studies, half-wave plates and polarizer were inserted accordingly in the incident ray path to achieve the required configurations.

The x-ray crystallographic studies of the samples with different Mg dopant are shown in Figure 1. In sample S1, the diffraction peaks confirmed the presence of monoclinic M1 phase of VO<sub>2</sub> (JCPDS # 04-007-1466). Whereas the diffraction peaks for sample S2 resembled the T phase of VO<sub>2</sub> (JCPDS # 01-071-0289). The samples S3 to S6 were identified as the M2 phase of VO<sub>2</sub> (JCPDS # 00-033-1441).

Eighteen Raman-active modes are predicted by Group theory for the low-temperature phases of VO<sub>2</sub> at  $\Gamma$  point (M1: 9A<sub>g</sub>+9B<sub>g</sub> and for M2 and T: 10A<sub>g</sub>+8B<sub>g</sub>). Twelve modes for sample S1, thirteen modes for sample S2 and eleven Raman modes for samples S3 to S6 (Figure 1b) are observed. Raman mode frequencies at 141, 190(A<sub>g</sub>), 221(A<sub>g</sub>), 258 (either A<sub>g</sub> or B<sub>g</sub>; A<sub>g</sub>/B<sub>g</sub>), 307(A<sub>g</sub>/B<sub>g</sub>), 335(A<sub>g</sub>), 391(A<sub>g</sub>/B<sub>g</sub>), 440(A<sub>g</sub>/B<sub>g</sub>), 494(A<sub>g</sub>/B<sub>g</sub>), 611(A<sub>g</sub>), 665(B<sub>g</sub>), 823(B<sub>g</sub>) cm<sup>-1</sup> in sample S1 confirmed the presence of pure M1 phase of VO<sub>2</sub>. In sample S2, Raman modes at 121, 201(A<sub>g</sub>), 225(A<sub>g</sub>), 267(A<sub>g</sub>/B<sub>g</sub>), 304(A<sub>g</sub>), 343(A<sub>g</sub>), 374(A<sub>g</sub>/B<sub>g</sub>), 409(B<sub>g</sub>), 440(A<sub>g</sub>/B<sub>g</sub>), 501(A<sub>g</sub>/B<sub>g</sub>), 572(A<sub>g</sub>), 636(A<sub>g</sub>) and 828(B<sub>g</sub>) cm<sup>-1</sup>, resembled with the reported data for T phase of VO<sub>2</sub>. For samples S3 to S6, the Raman peaks at 60, 203(A<sub>g</sub>), 216(A<sub>g</sub>), 225(A<sub>g</sub>), 271(A<sub>g</sub>/B<sub>g</sub>), 293(A<sub>g</sub>), 339(A<sub>g</sub>), 432(A<sub>g</sub>/B<sub>g</sub>), 450(A<sub>g</sub>/B<sub>g</sub>), 650(A<sub>g</sub>) and 831(B<sub>g</sub>) cm<sup>-1</sup>, matched with the reported M2 phase of VO<sub>2</sub>. XRD and Raman spectroscopic studies verified in the presence of three different phases of VO<sub>2</sub>, i.e., M1, T and M2 in samples

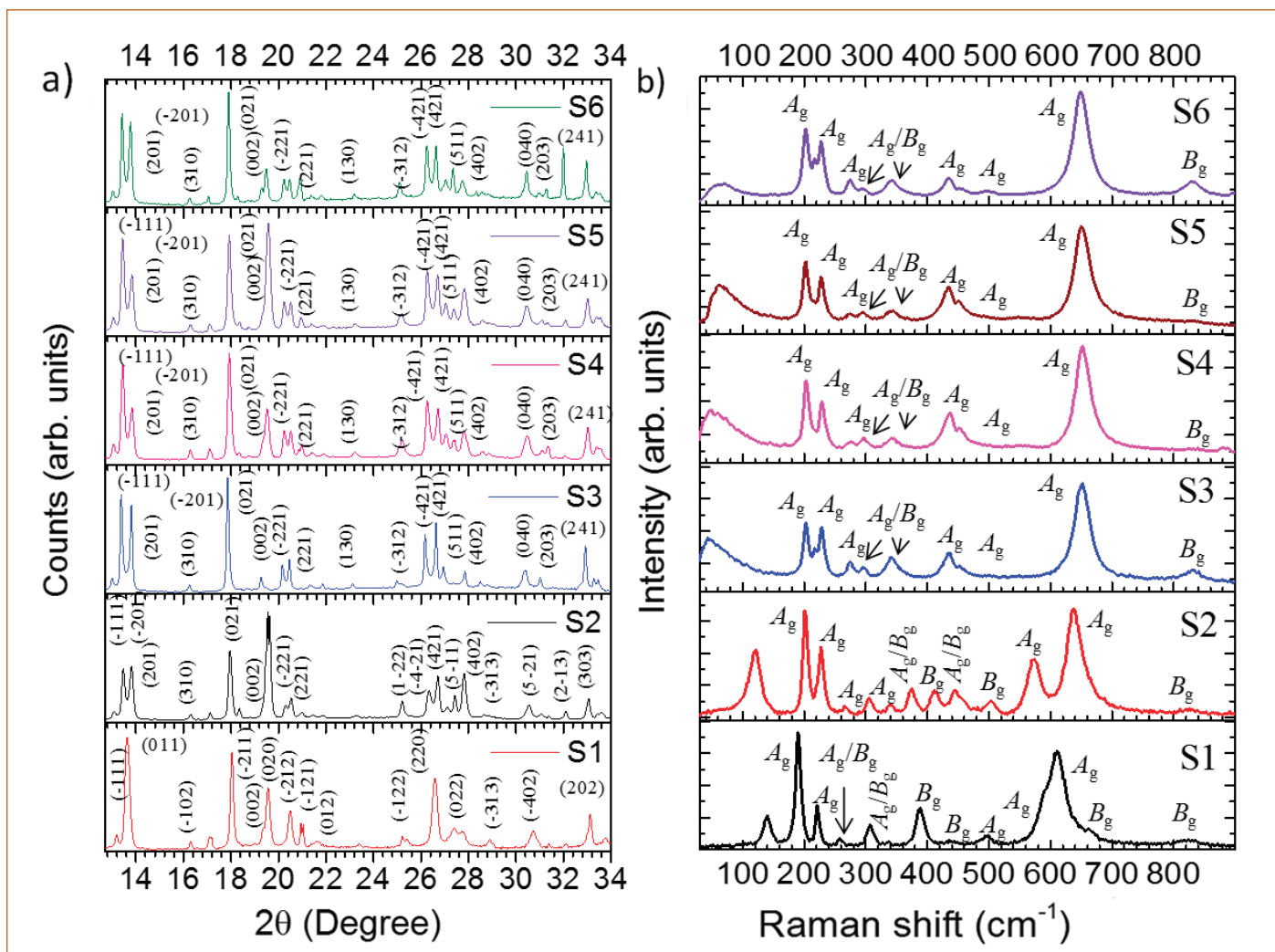


Figure 1: (a) The XRD pattern of the samples S1 to S6. The crystallographic (hkl) planes of the corresponding phases are indicated. (b) Raman spectra of the samples S1 to S6 collected at room temperature with corresponding symmetry notations

S1, S2 and S3 to S6, respectively. As, all the samples were grown on same substrate maintaining similar growth parameters except the carrier gas flow-rate, the existence of strain introducing via Mg doping might be the possible reason for the stabilization of T and M2 phases at room temperature in the samples S2 and S3-6, respectively. The Raman modes observed at 190 and 221 cm<sup>-1</sup> for sample S1 were assigned to the vibration of Vanadium ions along and perpendicular to the CR axis, respectively. These modes were observed at 201 and 225 cm<sup>-1</sup> for sample S2 and 203 and 225 cm<sup>-1</sup> for samples S3 to S6. The shift in frequency for the Raman mode ~190 cm<sup>-1</sup> for S1→S2→S3 transition is 13 cm<sup>-1</sup>, whereas the frequency shift for the mode ~221 cm<sup>-1</sup> is only 4 cm<sup>-1</sup>. The above observations imply that the doping of Mg introduces strain along CR axis and thereby stabilizing the T and M2 phase of VO<sub>2</sub>. The 141 cm<sup>-1</sup> band in sample S1 is reported as an external mode in one recent article, which can be viewed as relative motions of structural units with respect to each other. The mode is observed at 121 cm<sup>-1</sup> in sample S2 and ~ 50-70 cm<sup>-1</sup> for samples S3 to S6. The low-frequency Raman mode for samples S3-S6 shows a continuous blue-shift (inset of Figure 2a) with the increase in doping while the other Raman peaks do not show any shift in frequency (Figure 2a) with doping.

VO<sub>2</sub> is reported to consist of long chains of Vanadium ions along the CR axis, which can be considered as 1-D Heisenberg spin ½ chains,

since each V contains a single electron. The Hamiltonian for 1D spin ½ Heisenberg system can be written as,

$$H_0 = J \sum_j S_j \cdot S_{j+1} \dots \dots \dots (1)$$

where J (+Ve) is the exchange interaction. The Hamiltonian H<sub>0</sub> commutes with Raman operator R<sub>0</sub> and no Raman spectrum is expected for 1D spin ½ system. However, a perturbation v<sub>0</sub> due to static bond dimerization may exist as given by

$$v_0 = \sum_j J(-1)^j u S_j \cdot S_{j+1} \dots \dots \dots (2)$$

where u is the distortion. The effective Hamiltonian is given as,

$$H' = H_0 + \int dx/a_0 u d \sin(\sqrt{2}\pi\phi) \dots \dots \dots (3)$$

where x = ja<sub>0</sub>; a<sub>0</sub> is the lattice spacing and φ is the canonical part of Bosonic fields.

Equation (3) can be solved by Sine-Gordon (SG) model with three kinds of spinon excitations; soliton (S), antisoliton (S') and some breathers (Bn), which are the soliton-antisoliton bound states.

In SU(2)-symmetry, the soliton mass and second breather mass can be evaluated as

$$E_s \sim 1.5u^{2/3}J \text{ and } E_2 = \sqrt{3}E_s \dots \dots \dots (4)$$

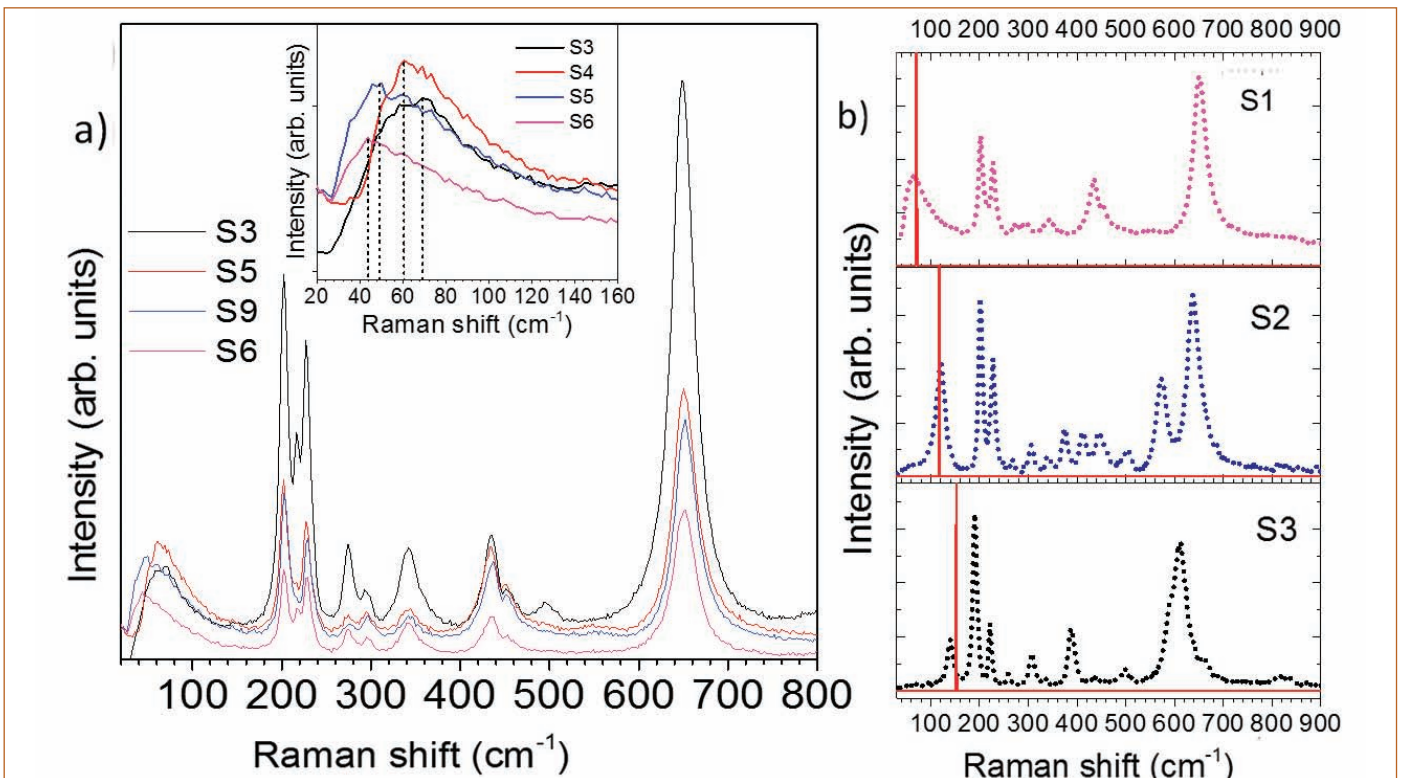


Figure 2: (a) Raman spectra for the samples S3 to S6. The inset shows Raman spectra for samples at lower frequencies. (b) Typical Raman spectra of all the samples S1, S2 and S3 and corresponding δ-functional peak at the calculated Raman mode frequency

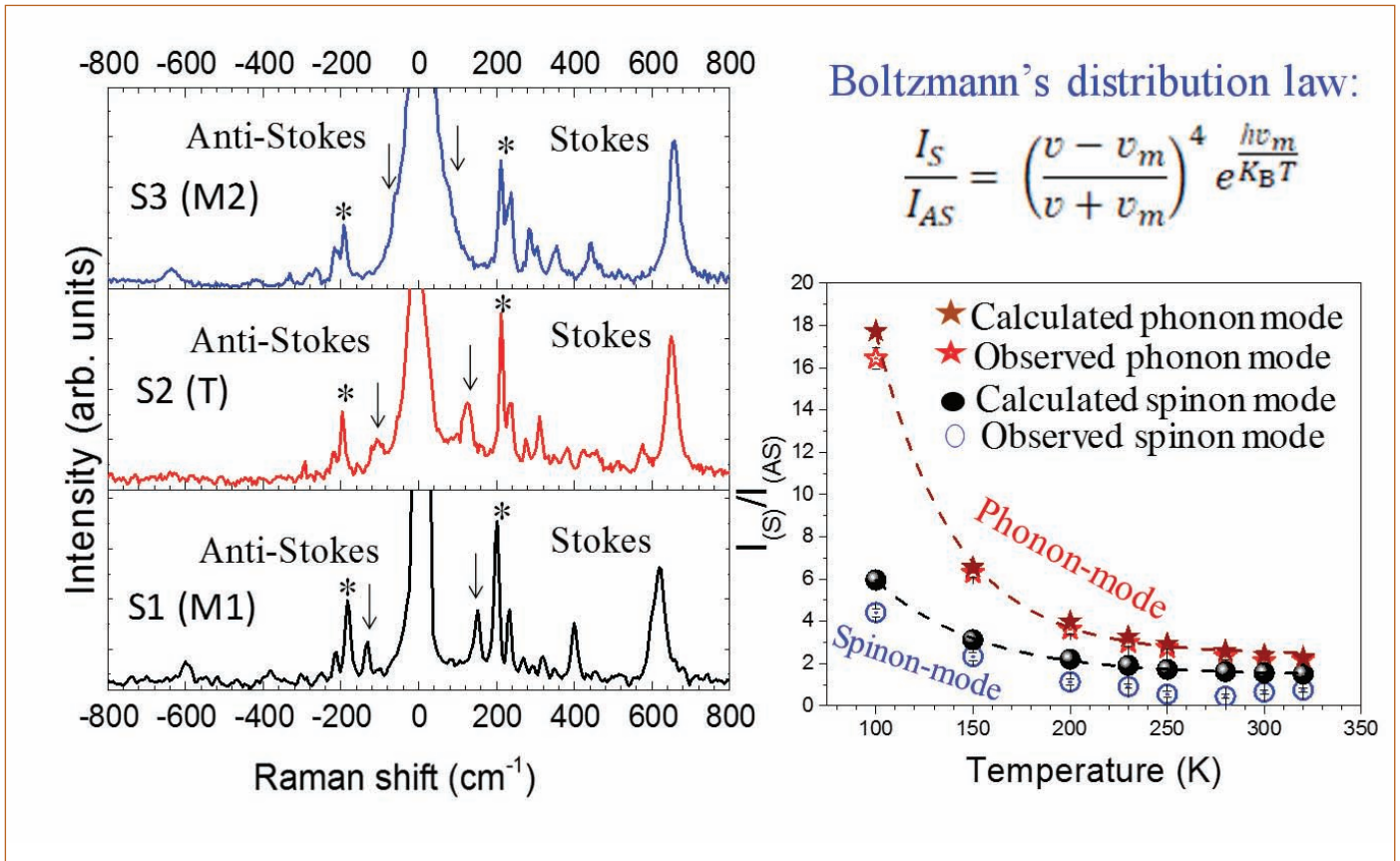


Figure 3: (a) Stokes and anti-Stokes spectra for the samples S1 (M1), S2 (T) and S3 (M2). The spin-wave and the phonon mode used for calculation of (IS/IAS) ratio are denoted by the arrow and '\*' sign, respectively. (b) The observed and calculated Stokes to anti-Stokes (IS/IAS) ratio for both phonon (indicated by '\*') and spinon modes with temperature typically for sample S1

In the SG model, the Raman spectra is observed in the low-frequency region; at  $\omega = E_2$ . Raman scattering from 1-D spin  $\frac{1}{2}$  chain is theoretically explored. It is reported that in the case of dimerized chain, Raman intensity due to the triplets gives rise to a continuum background at frequencies  $\omega \geq 2E_s$ . Spin singlet breather  $B_2$  appears as a  $\delta$ -functional peak at  $\omega = E_2$  using form-factor approach (provided  $T < J$ ). However, in a practical case, a broadening in  $\delta$ -functional peak is expected as the experiment is carried out at non-zero temperature.

The calculated distortion ( $u = \Delta/l$ , where  $l$  is the distance between two spins) for the three samples S1(M1), S2(T) and S3(M2) are  $u_1 = 0.07$ ,  $u_2 = 0.08$  and  $u_3 = 0.12$ , respectively. The values of  $J$  for the M1, T and M2 phases of  $VO_2$  are reported as  $\sim 500$  K,  $\sim 350$  K and  $\sim 320$  K, respectively, using nuclear magnetic resonance (NMR) studies. The Raman mode frequencies for the samples in M1 (S1), T (S2) and M2 (S3) phases are calculated using equation (4) as  $\omega_1 = 152$   $cm^{-1}$ ,  $\omega_2 = 117$   $cm^{-1}$  and  $\omega_3 = 66$   $cm^{-1}$ , respectively, which matches close to the observed low-frequency Raman modes. The calculated and experimentally observed peaks are shown in Figure 2b.

To reconfirm the origin of low-frequency Raman modes, the intensity ratio of the Stokes to anti-Stokes ( $I_S/I_{AS}$ ) Raman spectra for both the spin-wave and phonon vibration as a function of temperature are calculated. The Stokes and anti-Stokes Raman spectra collected at room temperature are shown in Figure 3a. The presence of spin-wave in both Stokes and anti-Stokes sides close to the Rayleigh line for all the three samples are denoted by an arrow mark. The frequency-shift, as well as the integrated  $I_S/I_{AS}$  ratio for the collective spin excitation at the lowest frequency and the closest phonon mode, originated due to V-V vibration  $\sim 200$   $cm^{-1}$  (denoted by '\*' in Figure 3a) are typically plotted as a function of temperature for sample S1 (Figure 3b).

The  $I_S/I_{AS}$  ratio is compared with the Boltzmann's distribution law (inscribed above Figure 3b), where  $\nu$  is the excitation frequency,  $\nu_m$  is the phonon frequency,  $h$  is the Planck's constant,  $k_B$  is the Boltzmann's constant and  $T$  is the temperature. It is clear from figure 3b that though there is a continuous red-shift with an increase in temperature for both the spin-wave and phonon mode, there is a significant mismatch between the observed  $I_S/I_{AS}$  ratio and the calculated one for the spin-wave (Figure 3b). However, IS/IAS

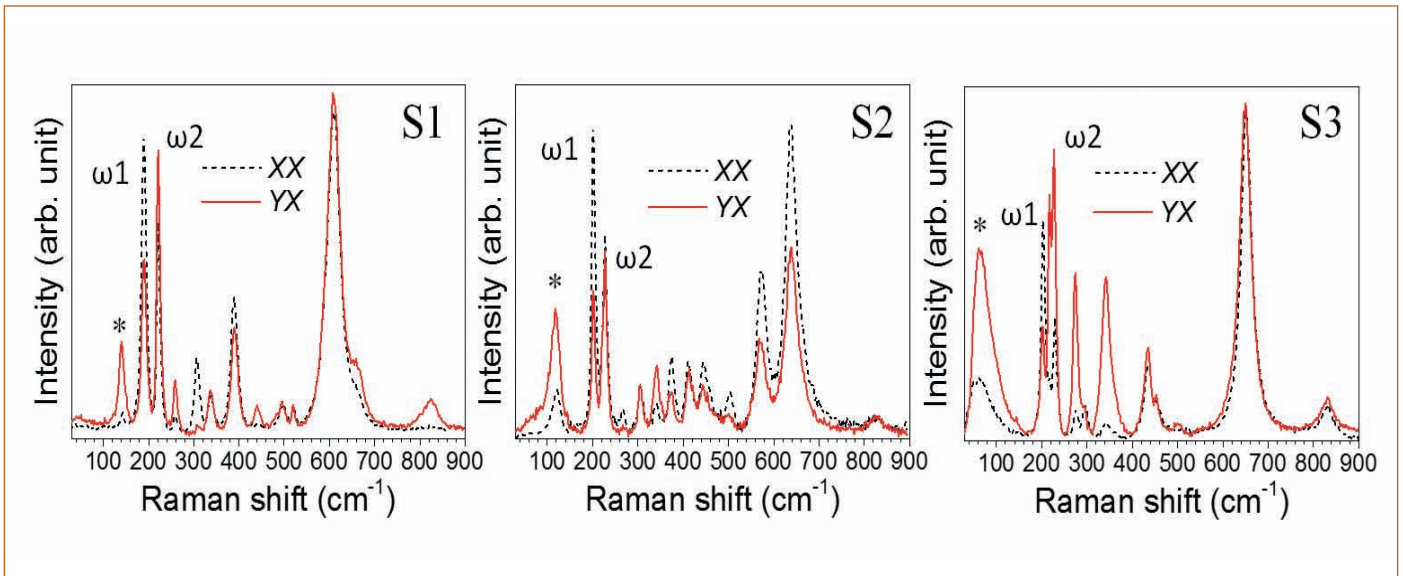


Figure 4: Raman spectra at parallel (XX) and cross (YX) polarization condition for the three samples S1, S2 and S3

ratio for the closest phonon mode  $\sim 200 \text{ cm}^{-1}$  follows the usual thermal factor of  $\exp(h\nu/K_B T)$  following Boltzmann's distribution law. However, the lowest frequency mode for all the three samples shows a considerable deviation of  $I_S/I_{AS}$  ratio from the usual thermal factor  $\exp(h\nu/K_B T)$  disobeying Boltzmann's law and thus confirming the mode to be originated from spin excitation.

The polarized Raman scattering on three single microrods of samples S1, S2 and S3 is carried out and the growth direction of the microrods ( $C_R$  axis) is chosen as the X direction, whereas the incident and the scattered light propagation direction is considered along the Z direction. The parallel,  $Z(XX)Z$  and perpendicular,  $Z(YX)Z$  polarizations were configured using a half-wave plate and a polarizer. The first and last letters in the Porto notation represents the direction of the propagation of the incident light ( $K_i$ ) and scattered light ( $K_s$ ), respectively and the second and third letter inside the parenthesis represents the direction of the electric field polarization of the incident light ( $E_i$ ) and the scattered light ( $E_s$ ), respectively. The Raman spectra for all the three samples are shown in Figure 4 with both parallel (XX) and cross (YX) polarization configurations. The intensity ratio between the Raman mode arising due to V-V vibration parallel to  $C_R$  axis (denoted as  $\omega_1$  in Figure 4) and perpendicular to the  $C_R$  axis (denoted as  $\omega_2$  in Figure 4) is more in the case of parallel (XX) polarization, whereas, the intensity ratio flips in the case of cross (YX) polarization condition. The above observation confirms that microrods are aligned along the X-axis, i.e., along the  $C_R$  direction. The intensity of the low-frequency Raman-modes is found out to be low in the case of parallel polarization ( $||$  to  $C_R$

axis) and increases rapidly for cross-polarization condition ( $\perp$  to  $C_R$  axis). As the spin chains are aligned along the  $C_R$  axis, the spinon vibration is expected to be produced parallel to the direction of  $C_R$ . In an electromagnetic wave, the electric field (E) and magnetic field (B) propagates orthogonally to each other. As the spinon vibration can be excited by the magnetic part of the electro-magnetic wave, the maximum intensity is expected for the cross-polarization (YX) condition; where E field propagates along the Y axis and B field propagates along X-axis. Thus the orthogonal dependency of the phonon and spinon vibration in the polarized Raman study confirms the origin of the low-frequency Raman modes as spin waves.

In conclusion, stable M1, T and M2 phases of  $V_{1-x}Mg_xO_2$  microrods were synthesized at room temperature via controlled doping of Mg. Strain along the  $C_R$  axis due to Mg doping is found out as the main cause for the evolution of the M1 phase into M2 and T phases. The structural phase stabilization is elucidated by the observed low-frequency Raman modes ( $\sim 50$  to  $140 \text{ cm}^{-1}$ ), which are found out to originate due to the dimerized spins and are compared with the calculated spinon vibrations. Moreover, it is found that the Stokes to anti-Stokes intensity ratio of the low-frequency Raman mode differs considerably from the Boltzmann's distribution law confirming it to be originated due to spinon vibration. Polarized Raman study was performed on the microrods to explore the crystallographic orientation as well as to identify the direction of spinon vibration. The orthogonal dependency of the phonon and spinon vibration in the polarized Raman study confirms the origin of the low-frequency Raman modes as spin waves.

## Measures related to COVID-19

In continuation of measures against COVID-19, following activities have been carried out by various groups.

### 1. Precautionary / preventive measures

- Health screening program to the employees and contract staff of IGCAR was conducted in two phases by Occupational Health Centre (OHC), SQ&RMG. Body temperature, SpO<sub>2</sub>, pulse rate, BP and other COVID-19 related symptoms were monitored and body immunity building medicines as prescribed by DAE hospital were distributed.
- Free groceries were distributed to about 50 poor families (RpG).
- RT-PCR test was made mandatory for migrant workers (FRFCF) on arrival at colony.
- Creation of quarantine area in labour colony (FRFCF) for migrant workers.
- A support group was formed with the following objectives:
  - ☉ To establish communication with the affected employees/their family members/their friends to provide necessary logistics and psychological support.
  - ☉ To take care of the day-to-day needs of the affected family and extend support to purchase vegetables, provisions, medicines etc.
  - ☉ To take adequate precautions to contain the spread of COVID-19.

### 2. Products Developed

Following UV sanitizers have been developed (at MCMFCG) and being used.

#### 1) UV Sanitizer chambers

Bench type UV-C sanitizer chambers were fabricated. The doors of the chamber are provided with manual & magnetic lock with limit switch. Safety controls ensures that lamp cannot be activated until the cabinet door is securely closed.



Hand held UV based area sanitizer

#### 2) Hand held UV based area sanitizer

Hand held UV-C radiation based area/room sanitizer, sterilizes the air & objects inside a room. It can sterilize surfaces at one meter distance in less than 5 minutes. It is fixed with a lamp which emits UV radiation that destroys the viruses. It can be used to cover a floor area of 6 sq. mtrs



UV Sanitizer chambers

## HBNI-IGCAR Corner

### Ph.D Thesis Defense

Name	Title	Date	Discipline
Ms. M. Divya	Weldability of borated stainless steel-SS 304B4	09/07/2020	Engineering Sciences
Shri G. Suneel	Numerical Modeling of Joule Heated Ceramic Melter	25/09/2020	Engineering Sciences
Shri G. Murali Krishna	Some Studies on the Electrochemical Behaviour of Actinides and Fission Products in Room Temperature Ionic Liquids for Nuclear Fuel Cycle Applications	16/09/2020	Chemical Sciences
Shri M. Mohideen Abdul Razak	Studies on PHWR Transients using Modified Exponential Time Differencing Method with Improved Quasi Static (IQS) Model and Associated Dynamic Sensitivity Analysis	16/09/2020	Physical Sciences

### Awards and Honours

**Ms. S. Sujee**, Stenographer, RMG/SQRMG, IGCAR was awarded **Consolation Prize** for Online Book Review Competition Conducted by Town Official Language Implementation Committee, Chennai on 13.08.2020.

## Biodiversity Basket - Avian Fauna

Black Kite



Photograph by SIRD

The Black Kite is a medium-sized raptor (bird of prey). From a distance, it appears almost black, with a light brown bar on the shoulder. It has long tails, strong toes, and sharply curved bills.

**Editorial Committee Members:** Dr. T. S. Lakshmi Narasimhan, Dr. N. V. Chandra Shekar, Ms. S. Rajeswari, Dr. John Philip, Dr. V. S. Srinivasan, Dr. C. V. S. Brahmananda Rao, Shri A. Suriyanarayanan, Shri M. S. Bhagat, Shri G. Venkat Kishore, Dr. Girija Suresh, Shri M. Rajendra Kumar, Shri S. Kishore, Ms. R. Preetha, Dr. N. Desigan and Shri K. Varathan.